NAZARBAYEV UNIVERSITY

School of Engineering and Digital Sciences

Bachelor of Engineering in
Mechanical and Aerospace Engineering

Investigation of Leading Edge Tubercles for Periodic 3D Wings with Flow Visualization Using PIV Laser

(Final Capstone Project Report)

by

Sabira Jussupbekova, Aruzhan Dauitova, Alikhan Bilyaliyev, and Adilet Irlanuly

Lead Supervisor: Prof. Altay Zhakatayev

Co-Supervisor: Prof. Basman Elhadidi

April, 2025

Declaration

We, Sabira Jussupbekova, Aruzhan Dauitova, Alikhan Bilyaliyev, and Adilet Irlanuly, hereby declare that this report, entitled “Investigation of Leading Edge Tubercles for Periodic 3D Wings with Flow Visualization Using PIV Laser” is the result of our own project work except for quotations and citations which have been duly acknowledged. We also declare that it has not been previously or concurrently submitted for any other degree at Nazarbayev University or elsewhere.

Signature: Sabira Jussupbekova Aruzhan Dauitov Alikhan Bilyaliyev Adilet Irlanuly

Name:

Date: April 30, 2025

Abstract

Particle image velocimetry (PIV) is a technique for visualizing the flow of particles. It has been used extensively to study different phenomena in aerodynamics, including vortex formation. Generally, there is plenty of research of airflow patterns during vortex formation at the tip of the airfoil. However, with advancements in research and technology, newer and more sophisticated flying apparatus have been developed in the past decades. For instance, quadcopters, wind-driven vehicles with propellers, and serrated wings to name a few. Flow patterns around these mechanisms are not studied sufficiently, since the mechanisms themselves were developed only recently. This study addresses the mentioned gap in research by obtaining airflow patterns around NACA 0012 wing profile, as well as the serrated wing by using particle image velocimetry. The methodology includes the experiment setup consisting of a wind tunnel, specialized camera, tracer particle generator, and PIV laser. PIV laser was set such that its rays reflected in a way that it could show the flow of particles around an airfoil. The tracer particle generator was set up in such a way that oil particles were plunged directly at the airfoil level, not higher than it and not lower. A mirror for reflecting laser beam and an adjustable table to fix and adjust the level of particle generator were added to the experimental setup later on to address some issues that arose during the experiment. Major findings of this research include visualization of the wing tip vortex of a NACA 0012 airfoil and the newly printed serrated wing profile.

Contents

List of Figures

Chapter 1

Introduction

1.1 Leading Edge Tubercles

The humpback whale (Megaptera novaeangliae) is one of the largest mammals in the world, yet it exhibits extraordinary maneuverability and agility despite its massive size. Its body is relatively inflexible due to specialized adaptations for lunge feeding, which imposes constraints on movement and turning ability [1]. To overcome these limitations, humpback whales rely on their highly mobile, elongated pectoral flippers, which function as biological hydrofoils to generate lift and enable sharp turns during feeding maneuvers [2]. Figure 1.1 shows the leading edge tubercles on a humpback whale flipper (left), the size of the flipper relative to the body (top right), and the flipper cross section (bottom right)[3].

Figure 1.1: Humpback whale and its flipper. Photographs: W.W. Rossiter.

A key feature contributing to the hydrodynamic efficiency of humpback whale flippers is the presence of leading-edge tubercles, protuberances that create a scalloped edge. These tubercles have been shown to delay stall, increase lift, and reduce drag at high angles of attack, enhancing the whale's ability to execute tight turns and rapid accelerations during prey capture [4]. Such adaptations are particularly crucial for feeding strategies like bubble-net feeding, where whales perform rapid banking turns to corral fish into concentrated masses [1]. The tubercles function similarly to vortex generators in engineered airfoils,

energizing boundary layer flow and maintaining lift under dynamic conditions [4].

1.2 Vortices and Aerodynamic Performance

Wing tip vortices are a significant phenomenon in aerodynamics, occurring at the tips of wings where high-pressure air from beneath the wing circulates into the low-pressure region above, creating distinct swirling patterns [5]. These vortices contribute to the induced drag and influence the overall aerodynamic efficiency of an aircraft. Understanding and visualizing wing tip vortices are essential for optimizing wing designs and improving aerodynamic performance.

Induced drag, a component of total drag, arises due to the lift generation and is inherently linked to wing tip vortices. As a wing produces lift, the high-pressure air beneath the wing spills over the tips into the low-pressure region above, creating swirling vortices that deflect the local flow downward [6]. This downward tilt of the lift vector relative to the free-stream flow results in a drag force parallel to the flight path [7]. The induced drag coefficient can be expressed as:

$$\mathrm{cD}_i = \frac{\mathrm{cL}^2}{\pi \cdot \mathrm{AR} \cdot e} \tag{1.1}$$

where cL is the lift coefficient, AR is the aspect ratio, and e is the Oswald efficiency factor (typically 0.7–0.9 for conventional wings) [6].

The lift coefficient (cL) and drag coefficient (cD) are critical parameters for evaluating wing performance. For a conventional NACA 0012 airfoil, which will be used in this paper, cL typically peaks near 1.2–1.5 at angles of attack around 12°–15° before stall occurs, while cD rises sharply post-stall due to flow separation [8].

The boundary layer, a thin region of viscous flow adjacent to the wing surface, plays an important role in determining the cL and cD coefficients. Laminar boundary layers, while low-drag, are prone to separation at moderate angles of attack, whereas turbulent boundary layers, although higher in skin friction, delay separation and maintain lift at higher angles [9]. The Reynolds number (Re), which depends on the flow velocity and wing size, determines the transition from laminar to turbulent. Re can be expressed as:

$$Re = \frac{\rho \cdot U \cdot L}{\mu} \tag{1.2}$$

where ρ is the fluid density, U is the flow velocity, L is the characteristic length (e.g., chord length for wings), and μ is the dynamic viscosity of the fluid. At lower Re, flow separation is more abrupt compared to higher Re regimes, where turbulence stabilizes the boundary layer [10].

1.3 Particle Image Velocimetry

Particle Image Velocimetry (PIV) is a widely recognized technique for visualizing and analyzing complex fluid flows. It offers significant advantages over traditional point measurement methods by providing instantaneous full-field flow velocity measurements with high accuracy. According to Hassan et al. [11], PIV is crucial for analyzing two- or three-dimensional complex flow fields and multiphase fluid flows. Its ability to capture unsteady flow fields without interfering with the fluid makes it particularly advantageous for studying phenomena like wing tip vortices.

1.3.1 Applications of PIV

The study of vortex rings and their interactions with various surfaces has provided valuable insights into the behavior of vortices. New et al. [12] investigated the collision of vortex rings upon V-walls, revealing the complexities in vortex dynamics depending on Reynolds numbers and surface configurations. Their findings highlighted the importance of factors such as included angles and boundary conditions in influencing vortex formation and propagation. While these studies primarily focused on vortex rings, they underline the importance of visualization techniques such as PIV to elucidate the behavior of vortices in different environments.

In terms of applications, PIV has been recognized for its effectiveness in studying turbulent flows. As Hassan et al. [11] noted, PIV has become increasingly popular due to its non-intrusive nature and its ability to capture detailed flow fields in real time. This makes it especially useful in aerodynamics, where understanding unsteady flow fields around objects like wing tips is critical. Scharnowski and Kähler [5] discuss the classical planar PIV techniques, highlighting their preference over the contemporary volumetric methods due to their versatility and adaptability for various applications. This adaptability makes classical PIV techniques suitable for capturing detailed images of wing tip vortices.

1.3.2 Challenges

Despite its advantages, implementing a fully operational PIV system can be challenging. At the beginning of this project, the PIV system available on our campus was not completely established due to the fact that it was barely used, which presented an opportunity to adapt existing PIV practices to specific wing profiles and wind tunnel conditions. By doing so, this project aims to obtain clear and informative visualizations of wing tip vortex structures. The potential of PIV in capturing such intricate flow patterns lies in its ability to provide both qualitative and quantitative data, which are crucial for understanding vortex behavior around wing tips.

1.4 Wing Profiles

Inspired by performance of biological structures like whale tubercles, this study compares the aerodynamic performance of a baseline NACA 0012 airfoil with the newly printed serrated wing profile with the wavelength of 20 mm to identify the most efficient design. By analyzing lift (cL) and drag (cD) coefficients, the paper evaluates whether tubercle-like serrations replicate the hydrodynamic advantages observed in humpback flippers. Such biomimetic applications could inform the development of high-performance wings for unmanned aerial vehicles (UAVs)[13],[14] or wind [**?**], where enhanced maneuverability and energy efficiency are critical.

1.4.1 NACA 0012 Airfoil

The first study object was a planform NACA 0012 airfoil, since it was ordinarily used in the university's wind tunnel for studies of different aerodynamic properties. It was generally a widespread object of study, so obtaining its wing tip vortex visualization was not something new in this field. In fact, it was a beginning of the research.

1.4.2 Serrated wing

The serrated wing was newly printed using Bambu 3D printer, with the wavelength of 20 mm. PLA filament was used as a material for printing the wing. The wing was studied in order to compare its aerodynamic performance with performance of planform NACA 0012 airfoil. Lift and drag were measured for both wing profiles. Moreover, vortices were visualized for both wings.

1.5 Aims

The main objective of this project is to utilize PIV to visualize wing tip vortices of NACA 0012 wing profile and of the newly printed serrated wing profile. By obtaining detailed images of these vortices, the aim is to enhance our understanding of their formation and characteristics. Such visualizations will contribute to our knowledge of aerodynamic phenomena and support the development of optimized wing designs.

Another objective includes setting up a PIV system in the wind tunnel on the university campus and making it fully functional. There is a PIV laser in the university's wind tunnel, but it needs to be calibrated to be fully functional, so that is one of the objectives as well.

The third objective of the experiment is to compare the aerodynamic performance of the NACA 0012 planform wing profile with that of the serrated wing. The lift coefficient and drag coefficient of the serrated wing profile are to be compared with the one of the NACA 0012 planform profile. That is how the best-performing profile will be discovered.

The problems encountered from these objectives are that: 1) the PIV system in a wind tunnel on campus was not fully established at the initial stage of the project; 2) there was a lack of results for wing tip vortices of a serrated wing using the PIV system.

This project aims to contribute to the field of aerodynamics by providing high-quality visualizations and analyses of wing tip vortices. Leveraging the capabilities of PIV, a deeper understanding of vortex formation is desired, thus informing future design and optimization efforts in aerospace engineering.

1.6 Outline

The rest of this report is organized as follows:

Chapter 2 follows Chapter 1 and displays the Literature Review.

Chapter 3 provides insights into Methodology used in order to achieve project aims

Chapter 4 demonstrates Results and Discussion section of the project

Chapter 5 presents Conclusions of the project

Chapter 2

Literature Review

2.1 PIV Technology

PIV technology was studied through literature review. Firstly, Scharnowski and Kähler implied that classical planar PIV techniques are preferred over contemporary time-based volumetric PIV techniques, and there are several reasons for this [5]. The working principle of a classical PIV technique is demonstrated and discussed in the article. The authors say that PIV can be tuned so that it has a wide variety of applications.

In another article on the application of PIV, Hassan and other researchers claim that PIV has numerous applications, and studying turbulent flows is one of the most demanding among them [11]. PIV has some advantages over other available techniques - for example, PIV does not affect the flow during operation. PIV is applied in different fields, but we are specifically interested in aerodynamics. PIV is useful in studying unsteady flow fields, which are not as easy to capture by other techniques. The generalized PIV setup is shown and explained in this paper [11].

In another article by Westerweel et al., it was also noted that studying turbulent flows is one of the most widespread applications of PIV technology [9]. The authors also expanded to explain how different types of PIV work. For example, the authors claimed that planar PIV can only be useful to determine the component of the instantaneous vorticity vector that is normal to the measurement plane, while stereoscopic PIV can be used to determine the three velocity components [9]. However, planar PIV has still been successfully used to measure vorticity [9].

2.2 Vortex Formation

Lot of research has been done on vortex formation. In his study about vorticity, Hunt claims that the general changes of vorticity and velocity are related to the movement of fluid-line elements [7]. Vorticity rolls up into vortices when fluid volumes are accelerated. Cylindrical volumes produce line-like vortices, while spherical volumes produce ring vortices [7]. The concept of vorticity was further developed by physicist William Irvine. His journey was described in the article by David H. Freedman [15]. Studying the vorticity and turbulence in water, he observed in one of his experiments that there are two interesting phenomena - writhing and twisting of a vortex ring. He also showed in his study that writhing can be converted to twisting, and that the vortex can actually untwist itself.

In another research connecting PIV technology and vorticity, Coletta et al. use the analysis of the velocity-gradient tensor and its three invariants for vortex visualization and compares it with some of the most popular vortex detection criteria [16]. The r_2 criterion presented remarkable results in terms of robustness and reliability on the real PIV data, in particular for the case of the strong laser reflection in the measurement region [16].

2.3 Vortex Structure Identification

The earliest methods for vortex formation identification include the Q-criterion, which is widely described in studies [7] and [17]. This method identifies vortices of an incompressible flow as connected fluid regions. Further advancements in vortex visualization techniques have been achieved through PIV. Coletta et al. [16] explored the application of the velocity-gradient tensor and its invariants to identify and characterize vortices in both theoretical and experimental PIV datasets. Their work demonstrated the robustness of the $r2$ criterion in detecting vortices even in the presence of strong laser reflections, making it particularly suitable for high-contrast flow visualizations like those required in this study.

Moreover, study by Graftieaux et al. also confirms that both $r1$ and $r2$ are robust functions when they are used in combination with proper orthogonal decomposition (POD) [18]. POD can separate contributions of turbulent flow and and unsteady swirling motion to the total energy, whereas $r1$ is a function for vortex center identification and $r2$ is a function for vortex core identification, which is essentially used for vortex boundary identification [18]. Angular momentum of the flow is a quantity the value of which cab be determined by using two abovementioned functions [18].

Studies on vortex rings, such as those by New et al. [12], provide complementary insights into vortex behavior. Their investigation into vortex ring collisions with V-walls highlighted the complex secondary and tertiary vortex formations influenced by Reynolds numbers and boundary geometries. These findings underline the importance of understanding boundary-induced vortex interactions, which are directly relevant to wing tip vortex behavior in constrained environments like wind tunnels.

2.4 Vortices and Aerodynamics in Biological Flight

Vortices play a crucial role in nature, with various insects, birds, and bats utilizing complex wing motions to generate leading-edge vortices (LEVs) and wake vortices, which help enhance aerodynamic performance. LEVs are critical for lift generation, particularly in slow and hovering flight, as seen in bats and insects [19] [20]. As Liu suggests, birds and bats can dynamically morph their wings to intensify LEVs, increasing vortex lift during maneuvers [19]. Moreover, LEVs are instrumental in high-lift generation in hovering

insects, stabilizing lift during flight [21]. Vorticity transport within the LEV is influenced by factors such as Reynolds number and wing aspect ratio, affecting lift production [21]. For instance, in hawkmoths, lift is produced through a combination of LEV attachment and vortex ring shedding during both downstroke and upstroke [22]. Whereas mosquitoes, with smaller stroke amplitudes, rely on added-mass forces and rapid pitching to generate lift, demonstrating different aerodynamic mechanisms compared to larger hoverers [23].

While wing shape, weight, size, morphology, and kinematics of different biological flyers (insects, birds, bats) together with different biological flight modes (hovering, forward flight) present considerable variability, the underlying principle in biological flight is vortex-induced unsteady flows. Understanding the complex mechanisms in achieving and controlling biological flight is concomitant with unveiling the interplay between vortex evolution and unsteady flow structures. The stable leading-edge vortex (LEV) is the prevalent unsteady aerodynamic mechanism in augmenting lift generation in flapping flight, applicable for insects, bats, birds, and all Reynolds (Re) numbers [19].

2.5 Serrated Wings

The aerodynamic performance of humpback-inspired serrated wings has been a subject of biomimetic research, with studies demonstrating that leading-edge modifications can improve lift-to-drag ratios and stall characteristics compared to conventional smooth-edged airfoils [2, 4]. Some useful papers were written on the study of serrated wings. In one of their studies, Hussain et al. [8] tried to identify the effect of trailing edge serrations on the lift and drag characteristics of NACA 0012 airfoil wing. The results showed that the implementation of square wave and stepped trailing edges reduces drag by up to 65 percent. Another study by Shorbagy et al. [24] focused on the aerodynamic performance of wings with and without tubercles similar to those humpback whales have on their flippers. The study included the effect of the Reynolds number Re and the sweep angle. The triangular wing with tubercles on the leading edge and an aspect ratio of AR = 2 was found to be the most sensitive to the increase in the Reynolds number. As the Reynolds number increased, the above-mentioned wing was able to gain 33 percent stall delay. The aerodynamic performance of the sinusoidal wing, another type of wing included in the research, was boosted by sweeping the wing back with 14 degrees. This manipulation increased the maximum value of the lift-over-drag coefficient ratio by substantial 46 percent. In addition, there was a 9 percent stall delay.

Shorbagy and his colleagues [24] also discussed some works of various researchers on different wing profiles. The study was focused primarily on the flippers of humpback whales. It is known that those flippers have some tubercles on their leading edge. Miklosovic et al. suggested that those tubercles might have interesting effects on the aerodynamics of humpback whale flippers. Together with his colleagues [4], Miklosovic

worked on two different models - one with a conventionally smooth leading edge, and another one with tubercles similar to the ones humpback whales have. The results were quite interesting; it turned out that the model with tubercles stalled 40 percent later than the conventional model with a smooth leading edge. Another study by Rostamzadeh et al. [25] was dedicated to investigating the effect of the Reynolds number on the mechanism of flow around the wing profiles with tubercles. The computational study was used by the researchers and it was found that there are stream-wise vortices present at the transition regime between laminar and turbulent regimes. The smoother stall was observed at transition regime due to the presence of such vortices. At turbulent regime, however, these stream-wise vortices seemed to cause the loss of lift. The effect of tubercles was also studied by Asghar et al. [26] They compared a conventional wing with a straight leading edge with the one with tubercles. The result was that critical value of the Mach number increased for the wing with tubercles. Cai et al. [27] studied the influence of tubercles on wings with the help of experiments and visualization of flow. They found that, at low angles of attack, the flow was symmetric and periodic, but at higher angles of attack the flow turned aperiodic on tubercles. The researchers explained this phenomenon by the occurrence of downwash on troughs of tubercles.

Custodio et al. [28] tested different models to study the effect of the wavelength and amplitude. The tests showed that the maximum lift coefficient decreased for the airfoils with tubercles, but the stall took place more gradually in comparison with conventional airfoils. The results also showed that the smaller the wavelength, the more gradual the stall, and the smaller the amplitude, the smaller the loss of the maximum lift coefficient.

An interesting finding was presented by Bolzon et al. [29]. They studied the wake around two different swept airfoils, with tubercles and without them. The results of the study showed that the tubercle airfoil had 2 vortices and one of the vortices was at least 4 times stronger than the other.

When it comes to the design of serrated wings, in the study [30] the baseline of the NACA0012 profile was used as the starting profile, while serrations were cut out of the leading edge of the wing. The researchers suggest that the amplitude and wavelength of the serrations should be within the range of 2.5-12 % and 10-50 % local chord lengths, respectively [30]. In this way, they are similar to the flippers of a humpback whale [30].

For vortex formation, evidence for LEV Modification DNS (Direct Numerical Simulations) and PIV studies directly shows that serrations induce streamwise and spanwise vortical structures at the leading edge, which either fragment or weaken the traditional large LEV, observed as reduced coherent vortex intensity and delayed flow separation [31], [32], [33]. The amplitude and wavelength crucially determine the degree of LEV fragmentation and stabilization ; larger serrations typically bring more pronounced LEV breakup than smaller or denser ones [33], [34]. At high AoA, serrated models sustain lift and delay stall, because the fragmented LEV delays breakdown, sustaining

reattachment over the wing surface[31], [34].

Chapter 3

Methodology

This research methodology consists of two parts: wing flow visualization using a PIV laser and a serrated wing aerodynamic performance assessment.

The first part of the methodology includes setting up an experimental wind tunnel environment with different wing sections and configuring the PIV system. The setup involves using tracer particles, laser illumination, and high-resolution imaging to capture the flow around the wing tips. Data processing, including cross-correlation techniques using MATLAB, will facilitate the extraction of velocity vector fields, offering a detailed representation of the vortex structures.

The second part includes design and printing of the serrated wing with the wavelength of 20 mm. The wing was designed in SolidWorks. Then, it was printed using Bambu printers. The design was adjusted for additive manufacturing constraints and the mounting that was suitable for use in the wind tunnel.

3.1 Experimental Setup

3.1.1 Experimental Equipment

The experiments were carried out in the AF1600 subsonic wind tunnel. The wind tunnel is 7515 mm long and has a 600 mm x 600 mm x 1250 mm working section, which is a closed visible part of the tunnel, where each side panel has a holder to support the wing models [35]. The air velocity in the working section is controlled by the speed of the axial fan, which has an electronic drive control unit. The operating velocity range is from 0 to 35 m/s.

The PIV system consists of a high-power laser for flow illumination, a set of optical components to guide and shape the laser sheet, and a high-resolution camera to capture particle trajectories. The LAS0404-LPY PIV laser produces visible 532-nanometer laser light, which is converted from infrared 1064-nanometer laser light [36]. The camera that is complementary to the laser was used in order to capture images. The camera has a filter. If it is installed, the camera can only see laser images, but not the usual light images that conventional cameras would capture. If the filter was removed, the camera would function as any other usual camera.

The seeding particles for PIV imaging are produced by olive oil smoke generated by the TSI 9307 Smoke Generator [37]. It consists of a control unit that pumps oil to the tip

of a probe. The oil is heated by a low voltage electrical coil at the probe tip, and the smoke trail is produced. The control unit allows adjustments to the intensity of the smoke to meet the requirements of air flow. The smoke generator works using a compressor that provides pressure of up to 7 psi. The mean droplet size was equal to 1 micron.

Later, during the experiments, another smoke generator was used. It is called the AFA10 Smoke Generator [38]. It works without a compressor. It is a smoke generator that is provided in conjunction with the wind tunnel. Its tube can be placed inside the working section of the wind tunnel by removing the window slot bung from the side window of the wind tunnel [38]. However, it was mostly located at the start of the flow, near the honeycomb structure of the wind tunnel to obtain images consistent with these already existing from experimenting with the previous smoke generator.

For initial experiment trials, the AF1600d Aerofoil of NACA 0012 (from this point onward called rectangular planform wing) was used. It has a symmetrical section and a span of 595 mm. For other trials, a serrated wing profile was selected and manufactured to examine how variations in design affect vortex formation and structure.

For later experiments, involving the serrated wing, the AF1600t Three Component Balance was used [39]. It was used to determine lift and drag generated by the wing at different angles and wind speeds. This equipment measures the angle of attack, lift, drag, and the wind speed using pressure sensors [35]. For analyzing and systematizing these data, VDAS software was used. It was pre-installed on the computer in the wind tunnel lab. It presents measurements of the AF1600t Three Component Balance in a user-friendly manner and allows to gather all of this information in Excel spreadsheets.

Moreover, there were some basic tools which were used in the setup. One of them was the black cover that was attached to the back of the wind tunnel. It has an important function: It absorbs the light from the back and does not let images taken by the camera be blurred by excessive light.

3.1.2 System Tuning and Calibration

Calibration and tuning of the PIV system were critical steps to achieve precise and reliable measurements. The camera and laser were positioned to capture the wing section plane with optimal clarity, with careful adjustments to the focal length, exposure time, and frame rate of the camera to reduce motion blur and enhance image resolution. The laser optics were aligned to create a uniform laser sheet at the wing section location (Figure 3.1).

Initially, only one mirror was used below the working section of the wind tunnel. It was used to reflect the laser light. Since the laser is heavy, it could not be lifted to great heights. The laser was placed on a big table with wheels. This means that the laser was at around 1 m height from the ground to be moved around easily. So, it was placed lower than the working area of the laser, and thus required reflecting laser beam above. That is why the mirror was placed at the bottom of the working section of the wind tunnel: it reflects the

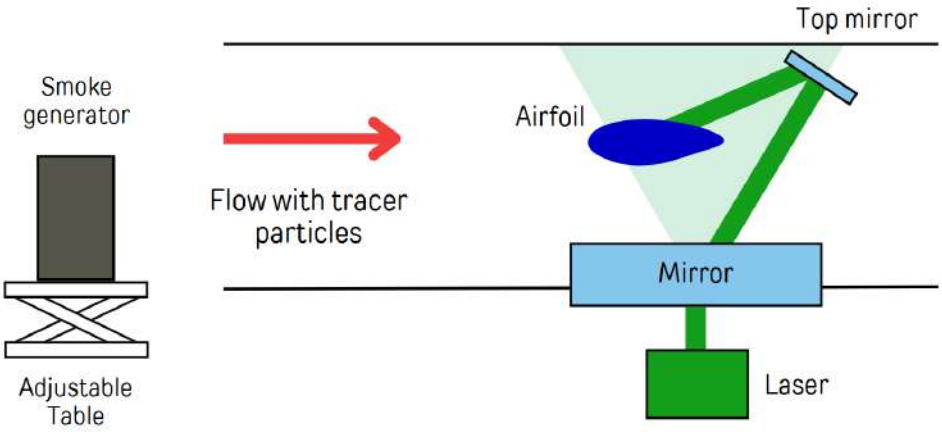

Figure 3.1: Final experimental setup

laser beam by 90 degrees, meaning that the laser sheet that was traveling horizontally below the wind tunnel would be redirected to travel from bottom to top, illuminating a wing section.

Aside from the bottom mirror, the top mirror was used in the setup. This was a design decision that was implemented in the first months of conducting the experiment. It was done because during first experiments the part of the section above airfoil was not illuminated by laser because of the shadow. Since the laser sheet was coming from the bottom, reflected from the bottom mirror, it could not reach the part of the section that was above the airfoil. That is why it was decided to reflect the laser sheet from the top of the wind tunnel to illuminate the part of the section above the airfoil. In such a way, the black shadow was eliminated. The mirror was placed in a holder (Figure 3.2). In fact, it was a phone holder that was repurposed to hold the mirrors at the top of the wind tunnel.

Figure 3.2: Mirror holder

The holder has a suction cup that holds the structure hanging from the top of the wind

tunnel (Figure 3.2). This suction cup can be easily attached to the surface or detached from it using a handle. It was convenient to attach the holder before beginning of each experiment and detach it at the end of it. Moreover, the lever at the top of the holder can rotate for 360 degrees. It was convenient to put it in any position that was required for the section depending on the distance from the airfoil to the holder itself. Two side supports and the bottom support are also movable. The width of the side supports is in the range of 70-96 mm. These dimensions are suitable for holding mirrors.

The lab grade mirrors of the company eisco were bought for this experiment for their good quality and outstanding reflective properties (Figure 3.3). Their length is 100 mm and width is 75 mm. They were stacked on top of one another length-wise and glued to the carton (Figure 3.2). That way, the coverage of reflected laser sheet was enlarged as much as it was possible.

Figure 3.3: Lab Grade Mirrors

The calibration was done using a QR code (Figure 3.4). It was done because QR code has many little black square parts and when camera is not focused properly, they cannot be seen properly. Only when the camera is focused the QR code is fully visible. QR code was put on top of the airfoil in order to focus the camera on the airflow. In fact, not only QR code, but all of the abovementioned tools were important for calibration. It was crucial to make sure that the bottom mirror, the top mirror, and the QR code were located on the same vertical plane at the wing section which was desired to be captured. Otherwise, the image simply would not be clear. A long ruler was used to ensure all three were at the same distance from the laser. After focusing the camera, QR code was taken away and camera captured pictures focused at the right plane, at the right place.

To further optimize the imaging results, a height-adjustable table was designed to ensure the smoke generator could deliver the tracer particles evenly across the laser sheet, providing consistent particle visibility within the flow field. The table was manufactured from several separately printed parts, as well as from some metallic parts provided by Technopark on campus (see Figure 3.5 below). The table design is shown in Figure 3.6. As it can be seen, the designed table operates on a scissor lift principle.

Figure 3.4: Calibration using QR code

Figure 3.5: Manufactured parts

The main motivation for building the table was the fact that the smoke generator should have been held at different heights at different wind speeds. There were multiple changes of wind speed during one experiment. At very low velocities, a person who was holding the table needed to keep the smoke generator low. That is why it was decided to build a table that could hold the smoke generator instead of a person having to hold it at different heights. The assembled table can be seen in Figure 3.7.

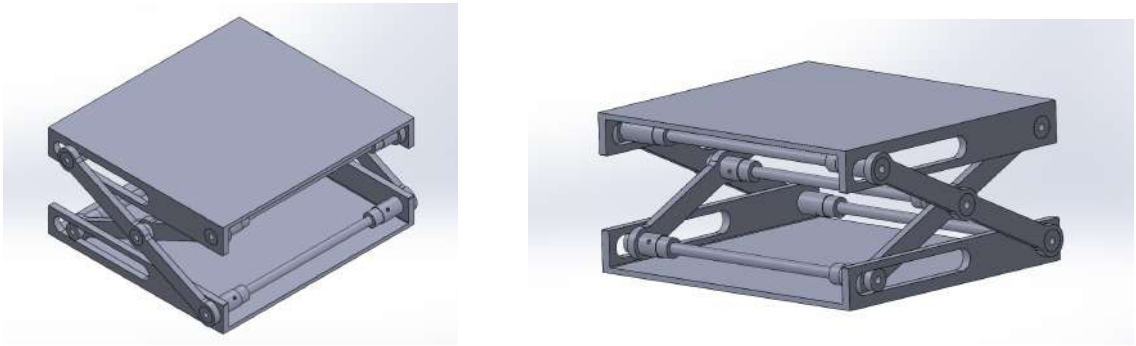

Figure 3.6: Height-adjustable table

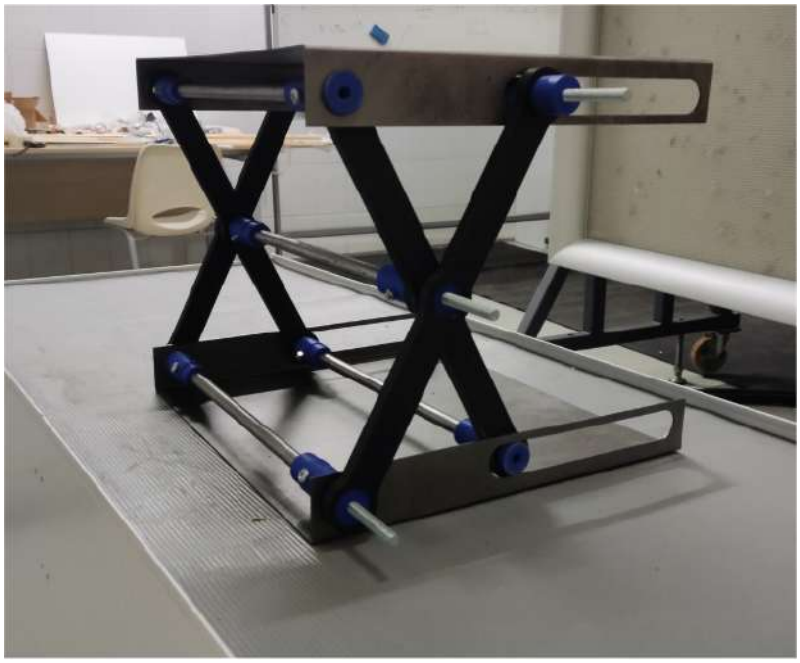

Figure 3.7: Assembled table

3.2 Vortex Visualization Procedure

3.2.1 Data Acquisition

For the laser visualization, the airspeed was set to 1.3, 2, 3, 4, 5, 6, and 7 m/s. The values were measured by the VDAS software from the pitot tube in the wind tunnel, which in some cases displayed fluctuating velocity values, so the interpolations were taken. The PIV system was activated to capture particle motion across the flow field. Multiple sets of images were taken to ensure reliable data, with particular attention given to capturing images near the trailing edge and the wake region where vortex formation was observed.

The experimental setup for PIV image capturing in the Insight 4G software was done according to the manual [40] (see Figure 3.8).

As it can be seen from the Figure 3.8, the capture was set to Sequence mode in order to capture several images. The number of captures was also adjusted to make sure that

Figure 3.8: Image Capturing Setup

several good-quality PIV images are obtained in a single run. Those good-quality images were then selected out of all the images captured. The captured images were preset to be saved to RAM (Random Access Memory) of the computer. The images were taken both for the regular NACA0012 planform wing and for the serrated wing. The design of the serrated wing will be covered in detail in Section 3.3.

3.2.2 Data Processing and Analysis

Following data acquisition, the raw PIV images were pre-processed to enhance particle visibility and remove any background noise. Image enhancements include contrast adjustments, which improve the clarity of the particle images, enabling more accurate tracking during analysis. Figure 3.9 features an original image and Figure 3.10 shows a pre-processed one.

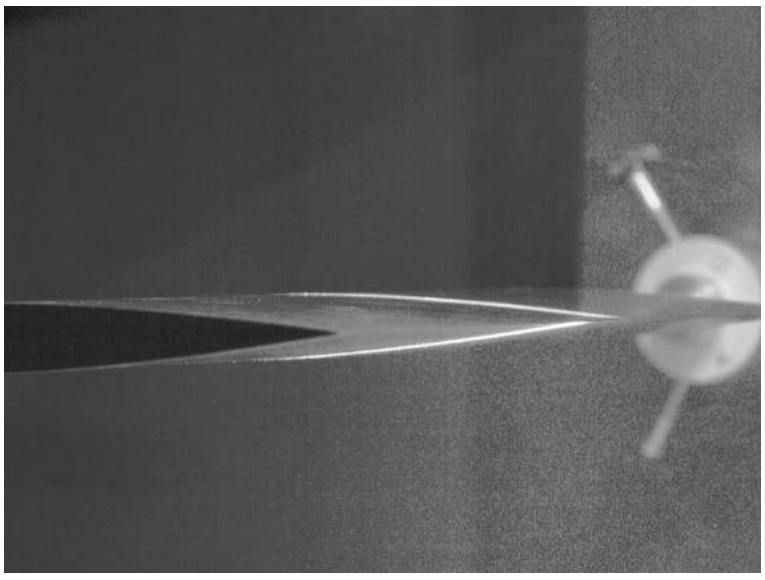

Figure 3.9: Original Image

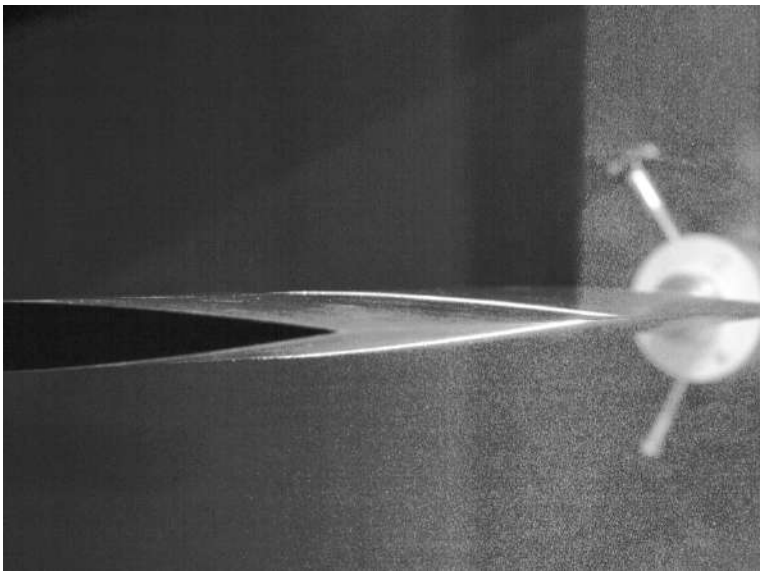

Figure 3.10: Pre-processed Image

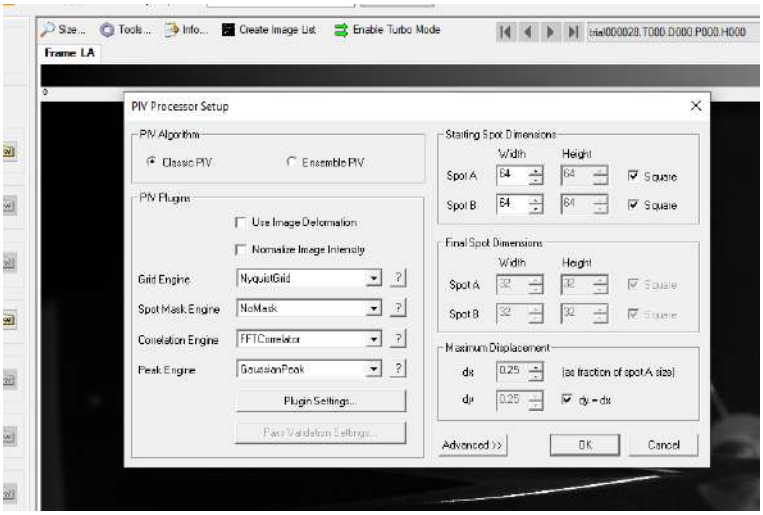

Figure 3.11: PIV Processor Setup

The velocity field analysis was performed in Insight 4G, and the setup is shown in Figure 3.11. The analysis begins with setting the grid, which is used to determine the spots to be processed, and the mask that defines the weighting to the displacement of which particles more value will be given. The next step was to choose a correlator that compares the particles depending on their shape and size. If the particle does not meet the correlator criteria, it will automatically be padded out of the interrogated region window. The result would produce the velocity vectors across the particles, with their direction represented by an arrow and a relative magnitude defined by the size of the arrow.

3.3 Serrated wing

3.3.1 Design of Serrated Wing

The serrated wing was designed in SolidWorks using the boundary feature. Two 2D airfoil profiles were drawn at a distance of 30 cm (wingspan). The trailing edges were connected with each other by a straight line. The leading edges were connected by a sinusoid. One serrated wing was designed for the purposes of this project. It has an $A = 5$ mm and a $\lambda = 20$ mm, which means it has 15 peaks and troughs throughout the wingspan (Figure 3.13). Both amplitude and wavelength were chosen according to [30]. The sinusoids were adjusted for the wavelength.

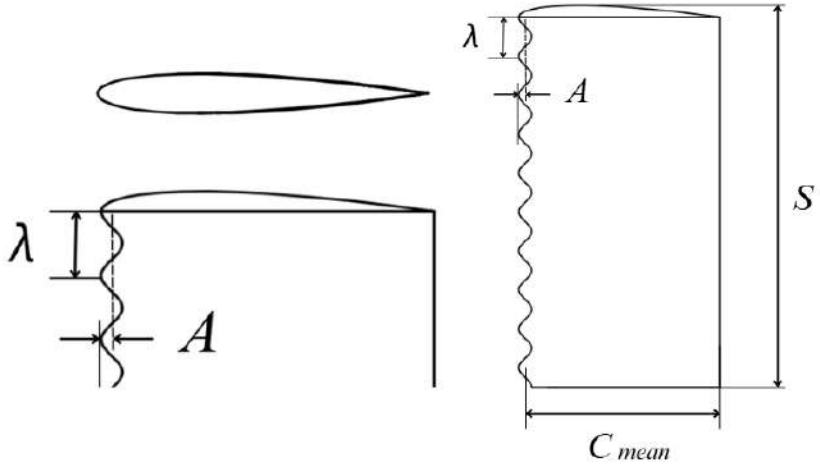

Figure 3.12: Serrated wing geometry

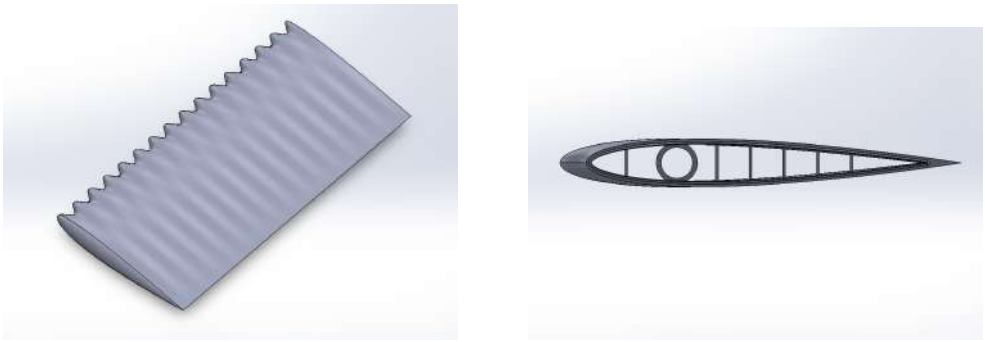

Figure 3.13: Serrated Wing Design with Wavelength = 20 mm

As it is presented in figure 3.12 above, the wing has a rounded part at the front. It was done in order to minimize unwanted excess vorticity at the front of the wing, which might have interfered with vortices at the section where it was aimed to capture them. Moreover, at the back view internal structure of the wing can be visible. Vertical rods were added to the internal structure of the wing in order to resist the external forces the wing might have faced in the wind tunnel. Initially, horizontal rods were also present in the design, however,

they were deemed unnecessary because the streamlined shape of the wing suggests that it can resist horizontal forces even without any internal structures. The cylindrical hole was made in order to fit in the rod that the wing would be mounted onto. The steel rod of diameter 12 mm was purchased for this research to mount the serrated wing onto it. This diameter was chosen because the existing planform NACA0012 airfoil is attached to wind tunnel's structure using rod of diameter 12 mm. That is why the wind tunnel's structure as well as three component balance's structure is manufactured to fit in the rod of diameter 12 mm.

The equation for the leading edge sinusoid:

$$y_{LE}(x) = A \cdot \sin\left(\frac{2\pi x}{\lambda}\right) \tag{3.1}$$

where A is the amplitude, λ is the wavelength, and x is the spanwise coordinate.

3.3.2 Additive Manufacturing

Additive manufacturing is basically 3D printing. 3D printing is used when there are some specific parameters to satisfy which are difficult to achieve using traditional machining. In the case of the serrated wing, 3D printing was truly the easiest way of manufacturing. Bambu printers for this project were kindly provided by our supervisor Altay Zhakatayev. PLA filament was used for printing as it was deemed most suitable.

First, two wavelengths were cut out of an entire wing. Fixtures were made on each of them for connection. One of the small parts had an extrusion of 4 mm, while the other had an extruded cut of 5 mm. It was important to know how the wing will behave in a cut state, because the wing ultimately had to be cut: the wingspan of the wing is 30 cm, while the height of the printer is 22.5 cm. Moreover, the cylindrical hole had to be made with a tight tolerance to the rod it was mounted on. For checking both connection between wing parts and the tight tolerance of the cylindrical hole, several attempts at printing were made (Figure 3.14).

As presented in Figure 3.14, there were four attempts to print the wing, of which three were unsuccessful, and only the fourth was successful enough to built a wing based on it. All the attempts presented in chronological order are placed from left to right on Figure 3.14. The first attempt had loose connections between the parts and the cylindrical hole could not fit onto the rod. The inner diameter of the hole was 12.1 mm, however, due to specifics of 3D printing it could not fit onto the mounting. Fixtures had 1 mm between each other.

At the second attempt, the connections were tighter. They had 0.15 mm between each other. That distance was chosen by assembly in SolidWorks. 0.15 mm was the smallest distance at which there was no interference in SolidWorks assembly. However, in real life it turned out to be too loose. The cylindrical hole was too loose as well. It basically

Figure 3.14: Attempts at Printing Serrated Wing

slipped through the rod. The inner diameter was chosen to be 12.3 mm this time. For the next attempt it was decided to make both connections and the cylindrical hole tighter.

First two attempts also lacked one important element. Both parts at those attempts were flat from one side and had fixtures on another side. That is why, it was convenient to just start printing them from the part where they are flat. However, in real model of serrated wing, parts of wing which are in the middle would have to have connections from both sides. That is why for the third attempt, parts which have connections from both sides were printed out. They had opposite type of connections on either side, meaning that each part had one extrusion and one extruded cut. That is how the small parts were able to be stacked up one after another. One more important thing to mention is that on the extruded cut side the parts have triangular "bridges" which go through all of the vertical rods and even through a cylindrical hole (Figure 3.15). It was done for convenience of 3D printing. If it was not for that bridge-like structure, the 3D printer, no matter at which connection the printing began, would have been required to start printing main internal structure of the wing on top of nothing. That happened because both connections provide some hollow shell without presence of any internal structures. If 3D printer is printing on top of nothing, it would lead to faulty results if the problem is not fixed. That is why the bridge-like structure was used on the inner structure of the wing: it provided smooth transition for 3D printer: from shell to growing internal structure.

This attempt was successful in terms of connections. The parts were printed such based on a 3D model where the distance between connections was zero. It was an ideal distance

Figure 3.15: Bridge like Structure for 3D Printing

because the parts connected to each other, because Bambu printer can print parts very exactly. However, there was still a problem with this version. The cylindrical hole was not fit tightly onto the rod. Even though it did not slide through the rod, when it was placed on the rod, it rotated around its axis. That meant that it could have unwanted behavior if it was placed into the wind tunnel. The inner diameter was equal to 12.2 mm.

For the fourth attempt it was decided to print the same connections, but change the inner diameter of the cylindrical hole to 12.15 mm. Each component was built with a bridge like structure at the extruded cut side. This attempt turned out to be successful. It satisfied all the criteria: it was easily printable, it was mounted onto a rod with a tight fit and the connections of the parts to each other were tight as well. 14 of these pieces were printed out for constructing the serrated wing.

3.3.3 Serrated Wing Performance Experiments

Prior to testing, the wind tunnel was calibrated with baseline measurements at zero airspeed and zero angle of attack to establish reference conditions. Two wing models were evaluated: a conventional NACA 0012 airfoil with smooth leading edges and a modified version featuring leading-edge serrations while maintaining the same base aerodynamic profile. Testing encompassed a comprehensive range of flow conditions, with airspeeds varying from 1 to 10 m/s.

For evaluation of the lift and drag characteristics changes with angle of attack, the

experiments for the set airspeed of 10 m/s were conducted. For the standard NACA 0012 configuration, measurements were taken at six discrete angles of attack: 0°, 3°, 6°, 8°, 12°, and 15°. The serrated wing configuration required more extensive characterization, with testing conducted across negative and positive angles ranging from -5° to +15° in 1° increments.

During each test run, the force measurements were recorded over a 30-second sampling period to establish stable mean values of lift and drag coefficients.

The cL and cD values were calculated for each AOA. Data validation included comparison of baseline NACA 0012 results with computational simulation as well as visual confirmation of flow quality using smoke visualization techniques at intermediate airspeeds.

3.4 CFD Analysis

The results of a CFD (computational fluid dynamics) simulation for a serrated airfoil represented by a NACA 0012 airfoil, with Re = 93,750 for angles of attack from 0 to 15° are presented in this study. For this simulation, the Detached Eddy Simulation (DES) with SST k-omega RANS model was used, and the fluid (air) was modeled as an incompressible gas. As for the boundary conditions, the inlet velocity was set to 10 m/s, the pressure-outlet was set to 0 Pa, and no slip condition was applied to the domain boundaries. The mesh was generated to be finer closer to airfoil (Figure 3.16).

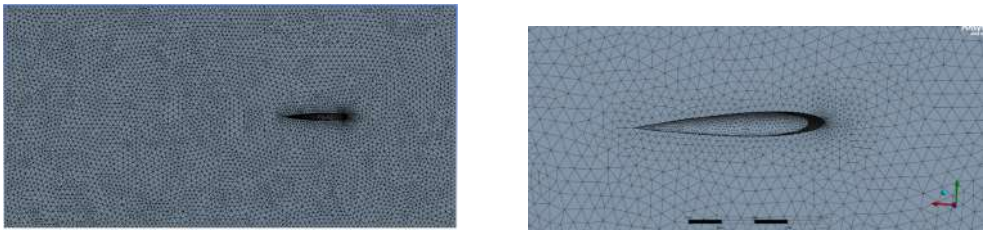

Figure 3.16: Mesh

Chapter 4

Results and Discussion

4.1 PIV System Setup

The PIV system setup was one of the primary aims of the project, and it successfully completed. The optimal position of the camera and PIV laser was found, and the focus of the camera was adjusted. The bottom and top mirrors were positioned so that the laser sheet was correctly reflected at the desired plane, and the release of the optimally dense smoke was achieved due to the introduction of the adjustable table. The schematic drawing of final experimental setup can be seen in Figure 3.1 in Methodology.

4.2 Flow Visualization

4.2.1 Rectangular planform Wing

The images included in the report were captured during several separate laboratory sessions. With the camera focusing properly, some clearly visible PIV images of the flow of the smoke particles around a rectangular planform NACA0012 wing profile and of the serrated wing of the same profile were captured in the Insight 4G software. The images were inverted and colored, and they were captured at different wind speeds - at 1.3 m/s, 2 m/s, 3 m/s, 4 m/s, 5 m/s, 6 m/s, and 7 m/s (see Figure 4.1).

The Figure 4.1 represents flow visualization of rectangular planform wing. The velocities were set using VDAS program. The wind speed in the wind tunnel is adjusted by rotating a knob, so the speeds given are not exact, but rather an average of the speeds that was measured by VDAS software when the wind tunnel was working. Moreover, as it was specified earlier, the PIV images were inverted and colored to achieve better visibility. An example of non-inverted images is shown on the Figure 4.2 It presents flow visualization around a rectangular wing at wind speed of 4 m/s. The rest of the non-inverted images corresponding to the Figure 4.1 are in the appendix.

Evidently, the flow at 1.3 m/s is laminar (Figure 4.1). The flow observed on the figure 4.1 is straight, it has no turbulence and no vortex. Flow at wind speeds from 2 m/s to 4 m/s (Figure 4.1) most likely present transitional flow, because even though some mushroom shaped vortices are seen, flow is still smooth. Flow at windspeeds from 5 m/s to 7 m/s (Figure 4.1) present a turbulent flow. As well as flow at lower speeds, it has mushroom

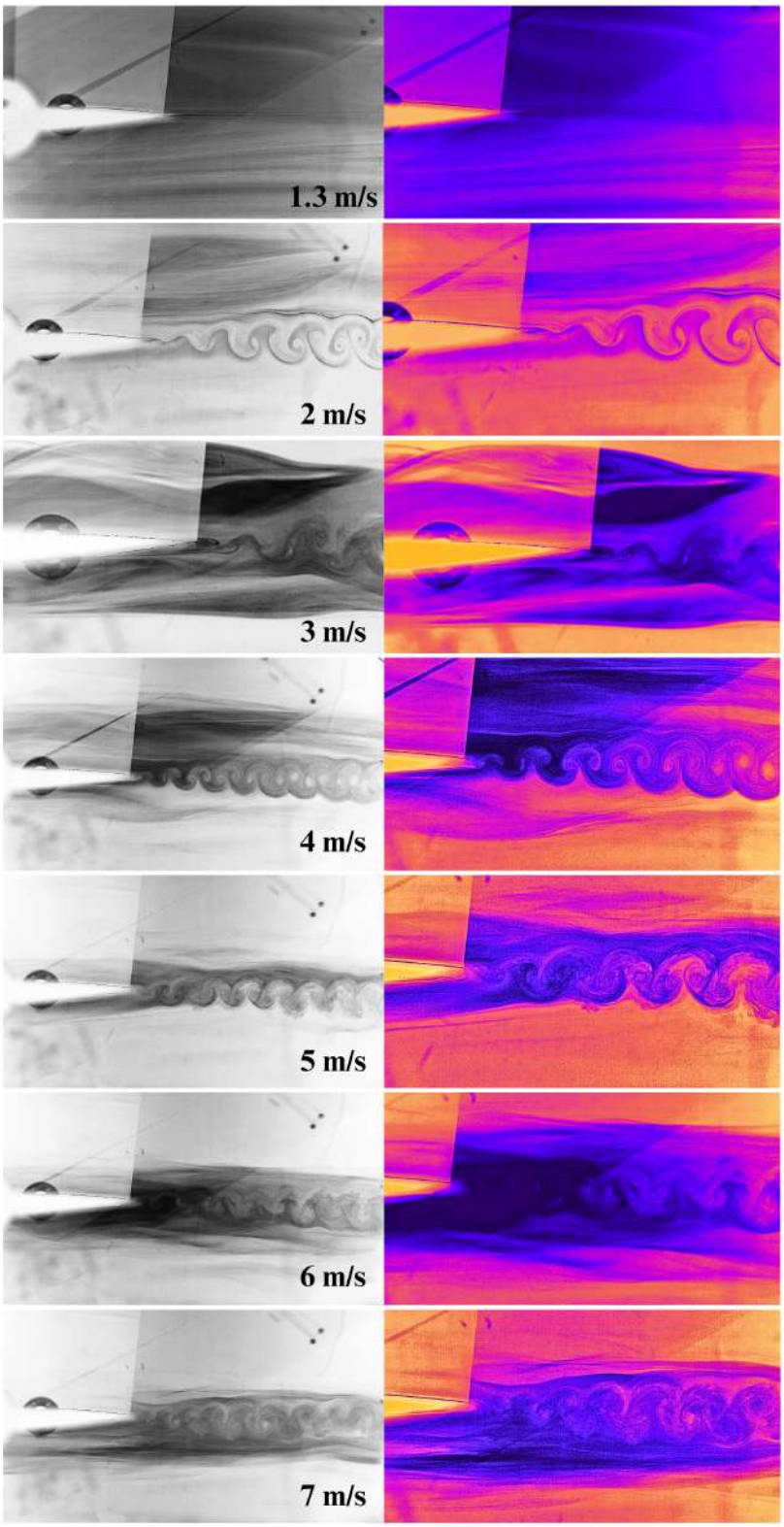

Figure 4.1: Particle flow around the rectangular planform wing at 1.3-7 m/s

shaped vortices. However, unlike flow at lower speeds, there are eddies clearly visible at the top of the mushrooms. This indicates highly turbulent flow.

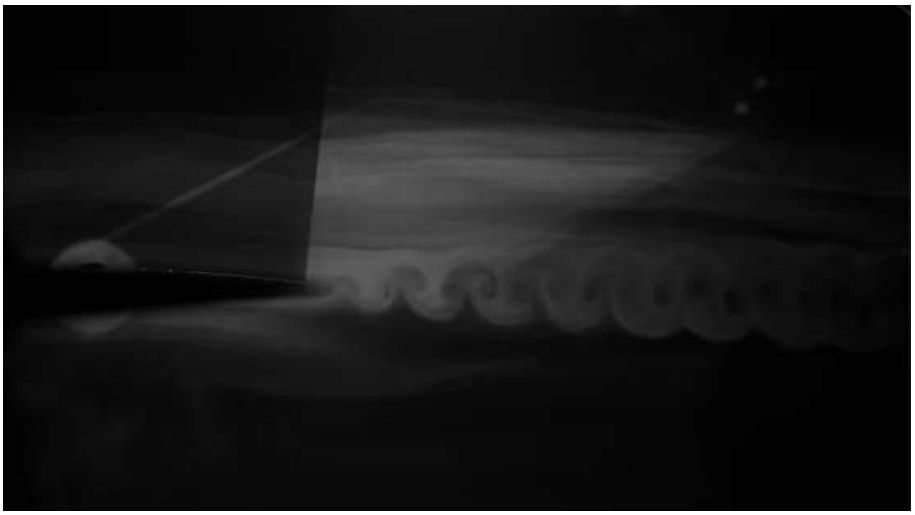

Figure 4.2: Non-inverted PIV image of the particle flow at 4 m/s

4.3 Serrated Wing

Images of flow around serrated wing were taken using the same setup. The images were taken at wind speeds of 2 m/s, 3 m/s, 4 m/s, 5 m/s, 6 m/s, and 7 m/s (see Figure 4.3)).

As it can be evident from the Figure 4.3, flow around the rectangular planform NACA0012 wing and flow around the serrated wing of the same base profile are similar. The flow around the serrated wing enters the turbulent phase at wind speed of around 5 m/s, same to the flow around the rectangular wing. It is apparent from the eddies at windspeed of 4-6 m/s on Figure 4.3. The shape of the vortices is also same for both cases: the vortices are mushroom shaped (Figures 4.1- 4.3). Another similarity of both cases is that the flow at 2-3 m/s has bigger vortices than flow at larger speeds (Figures 4.1- 4.3). Possible reason for that is transitional phase to which flow at lower speeds is attributed.

The difference between flow around rectangular planform wing and flow around serrated wing is the fact that the vortices in the flow around the rectangular wing are more defined and straight, while the vortices in the flow around a serrated wing are inclined towards the wing. It can be observed very clearly at the speed of 2 m/s on Figure 4.3. That may have been caused by the features of the serrated wing, as leading-edge serrations on fixed wings modulate LEV formation fragmenting the LEV into smaller structures, thereby delaying stall[31], [32].

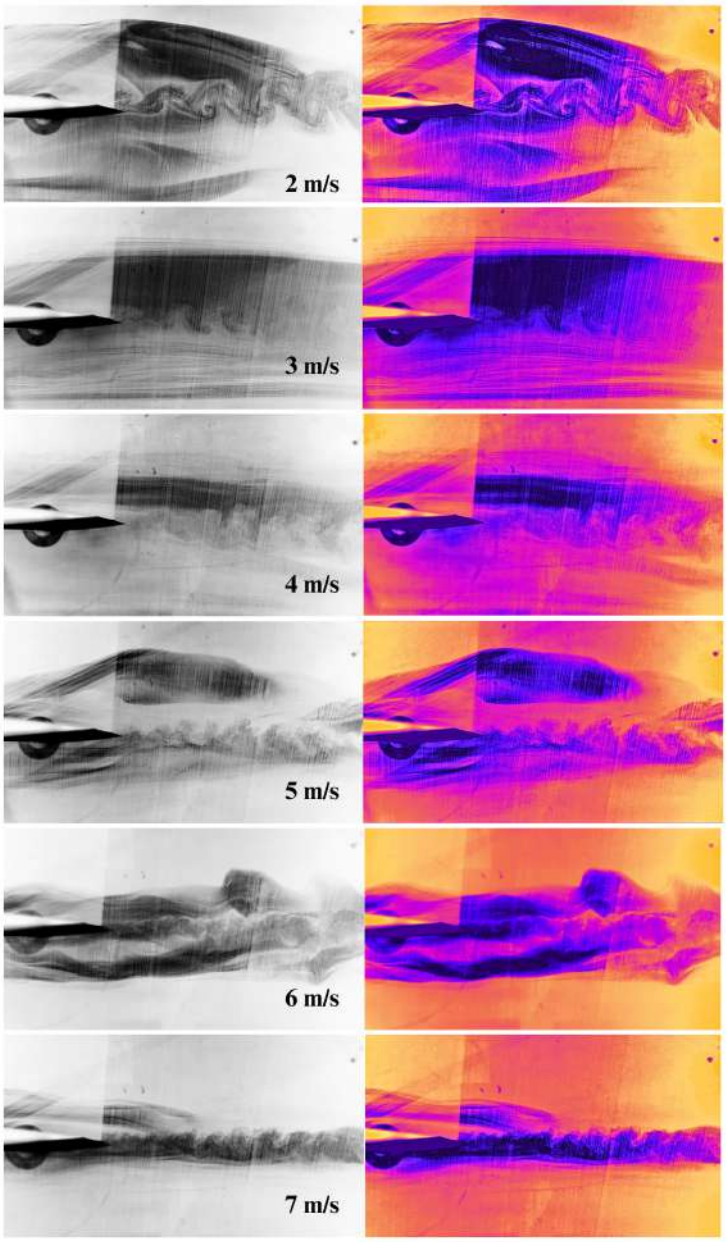

Figure 4.3: Particle flow around the serrated wing at 2-7 m/s

4.4 Flow Visualization at an Angle of Attack 5°and at the Wingtip

4.4.1 Flow Visualization at an Angle of Attack of 5°

In the previous two sections the flow visualization was done for the angle of attack equal to zero. In this section, the flow at an angle of attack of 5°was visualized for both fixed and serrated wings using the same setup. The expectation was that vortices at flow around wing would be more prominent at the angle of attack of 5°than at zero angle of attack. The visualization of flow around both fixed and serrated wing can be seen on Figure 4.4.

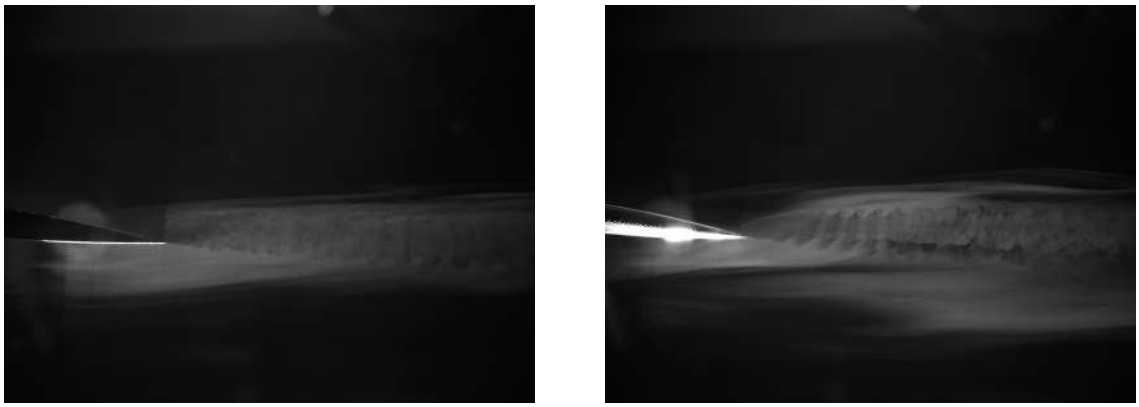

Figure 4.4: The flow around fixed wing (left) and serrated wing (right) at windspeed of 5 m/s and angle of attack 5°

The results show that vortices are indeed more prominent, and thus the wake region is wider at angle of attack 5°than at zero angle of attack for both fixed wing and serrated wing. Also, at angle of attack equal to 5°wake region of serrated wing is bigger than that of fixed wing. The trend of inclined mushroom shaped vortices is still true for serrated wing at angle of attck of 5°, however it is less prominent than at zero angle of attack because of wider wake region.

4.4.2 Flow Visualization at the tip

For tip vortex visualization, the serrated wing profile was tested at angles of attack of 0° and 5° with a testing velocity of 5 m/s. The wing has a rounded tip, and the flow patterns near the tip were analyzed.

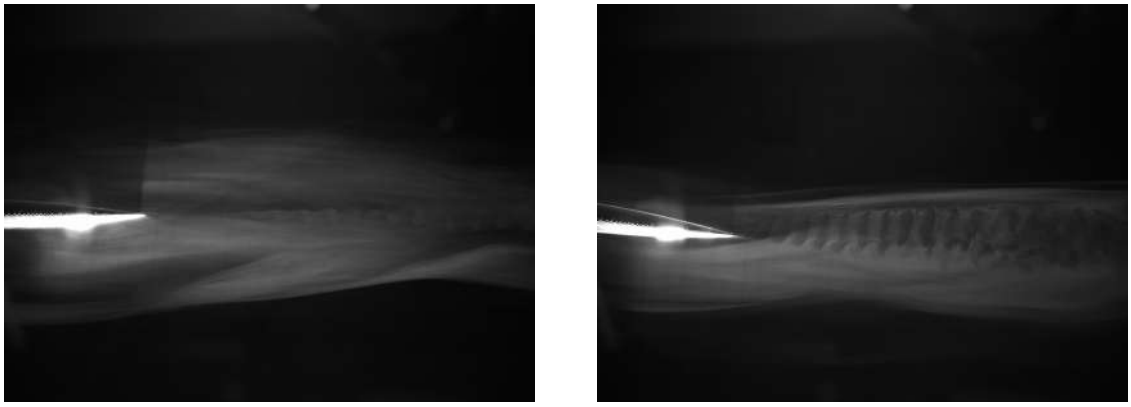

Figure 4.5: The flow at the tip of the serrated wing at 0°(left) and 5° (right) angles of attack 5°

As observed in the results shown in Figure 4.5, the tip vortex that begins to form at the wingtip shows distinct characteristics at different angles of attack. At 0°, the vortex is relatively small and not very prominent, which is expected since no lift is generated from the symmetric NACA0012 airfoil at this angle[41]. The formation of vortices depends

heavily on lift generation, which is minimal at 0°. However, at 5°, the vortex becomes more prominent. This can be attributed to the increase in lift generated at this angle, leading to stronger vortex formation and enhanced vortex strength. This supports the observation that vortices are directly influenced by the lift force generated by the airfoil, as higher angles of attack promote the formation of larger vortices.

The visualized data underlines the importance of understanding the role of angle of attack in vortex generation and highlights how such vortices, starting from the tip, evolve under different aerodynamic conditions. These findings align with previous studies on tip vortices, such as those by Uzun et al. [42], which demonstrated the complex dynamics of vortex formation around rounded wing tips using large-eddy simulations. The current experimental observations provide valuable validation for such numerical studies while offering insights into the practical implications of vortex behavior for aerodynamic performance.

4.5 Velocity Field Analysis

Despite obtaining high-quality images from the PIV system, the initial velocity field analysis was unsuccessful, as can be seen in Figure 4.6. This failure was likely due to two primary factors: the overseeding of tracer particles and their relatively small size.

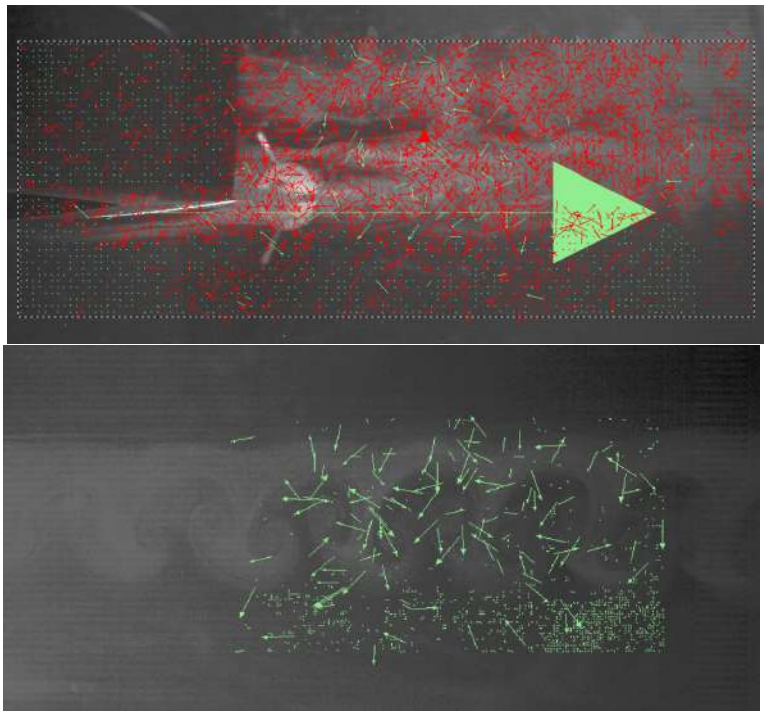

Figure 4.6: Failed velocity vectors (left) and improved version(right) of the flow field around rectangular wing profile

Overseeding occurs when an excessive number of tracer particles are introduced into the flow [40]. While seeding is necessary to track the motion of the fluid, too many particles

can lead to signal interference and noise in the captured images. This phenomenon reduces the clarity of individual particle movements, making it difficult for the cross-correlation algorithms to accurately calculate displacement vectors. Overseeding also increases the likelihood of particle overlap [40], further complicating the ability of the PIV software to distinguish individual particles.

The problem of overseeding was partially solved by calibration of pressure regulation in the smoke generator. Two types of smoke generators were used to obtain less dense flows suitable for velocimetry analysis.

4.6 Aerodynamic Performance Analysis

The aerodynamic performance analysis was conducted for the serrated wing and planform wing at the wind speed of 10 m/s. Initially at zero angle of attack (AOA = 0), the lift coefficient cL was equal to about 0.1 and the drag coefficient cD had a lower value of approximately 0.02. As the angle of attack increased, both lift and drag coefficients started to rise, the lift coefficient rising faster than the drag coefficient. When the angle of attack increased from 7 degrees to 8 degrees, the rapid growth of the lift coefficient was observed, which can be clearly seen from the graph (see Figure 4.8).

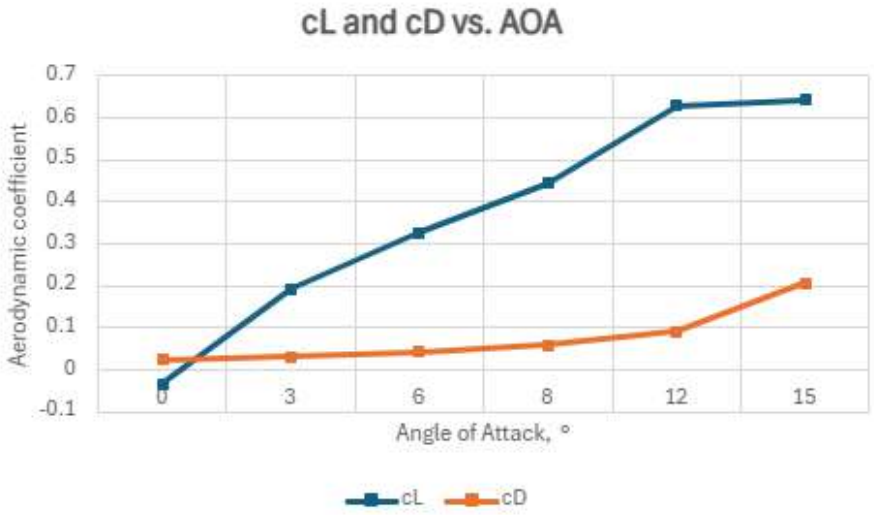

Figure 4.7: Lift coefficient and Drag coefficient of Rectangular Planform Wing over Angle of Attack

Lift-over-drag ratio was equal to 4 at zero angle of attack. As the angle of attack increased from 0 to 4 degrees, the L/D ratio also increased up to 7.5 (see Figure 4.9). It remained stable up to the angle of attack of 5 degrees before slightly rising again as the angle of attack rose from 5 to 6 degrees. After that, there was a gradual decrease of the L/D ratio up to the final angle of attack of 15 degrees. Looking at the graph of ratio of lift to drag against angle of attack, one might question the reliability of the graph because of the unexpected values it is presenting. Firstly, the large difference between lift and drag at

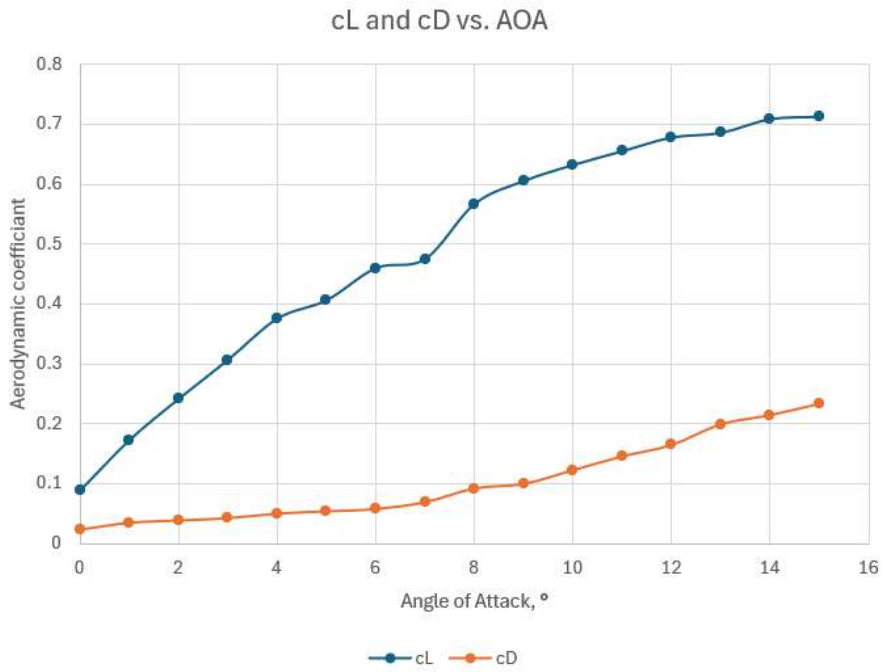

Figure 4.8: Lift coefficient and Drag coefficient of Serrated Wing over Angle of Attack

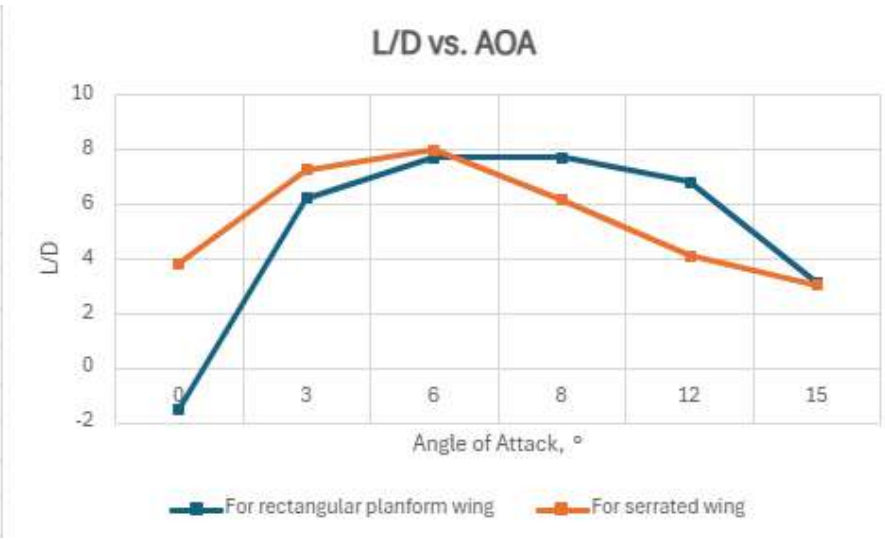

Figure 4.9: Ratio of lift to drag vs Angle of Attack for both wings

zero angle of attack is likely an outlier, because the wing is mounted onto three component balance by a person, and thus the zero angle of attack is defined by a person, which means that there was a chance of human error. The reliability of the lift-to-drag ratio graph is also affected by measurement uncertainties, particularly in the angle of attack. The angle of attack was manually set using a protractor, introducing potential alignment errors due to parallax or imprecise leveling, which could explain irregularities in the data—such as unexpected negative lift at low positive angles. These compounded uncertainties suggest that the case of the rectangular planform rectangular fixed NACA0012 profile wing is an outlier, since lift at positive angle of attack and wind speed equal to 10 m/s should not be

negative.

To better visualize the aerodynamic performance of the wings, the curves for both the rectangular planform wing and the serrated wing were included in the same plots (see Figures 4.9- 4.11). It can be inferred from the obtained plots that the rectangular wing, for example, reached the peak value of lift-to-drag ratio at an angle of attack of 8 degrees, while the serrated wing reached the peak earlier at 6 degrees AOA. At higher angles of attack, the gradual decrease of lift-to-drag ratio was observed for both wings (Figure 4.9).

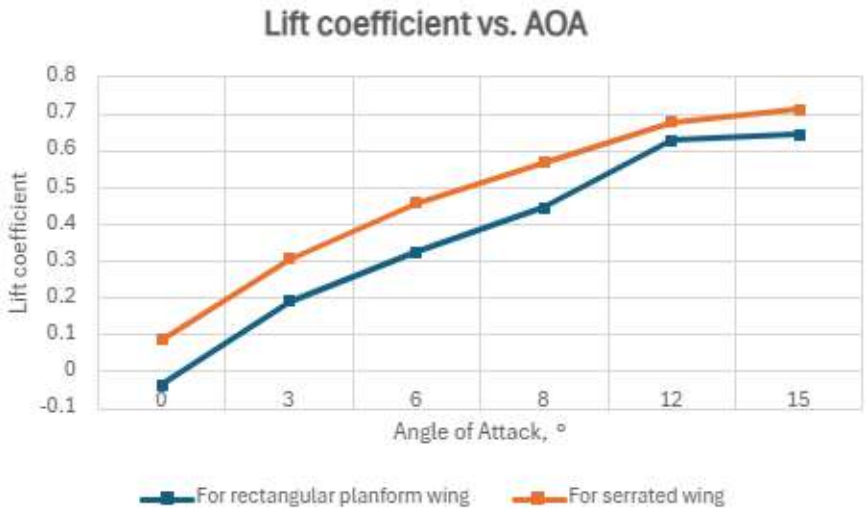

Figure 4.10: Lift coefficient vs Angle of Attack for both wings

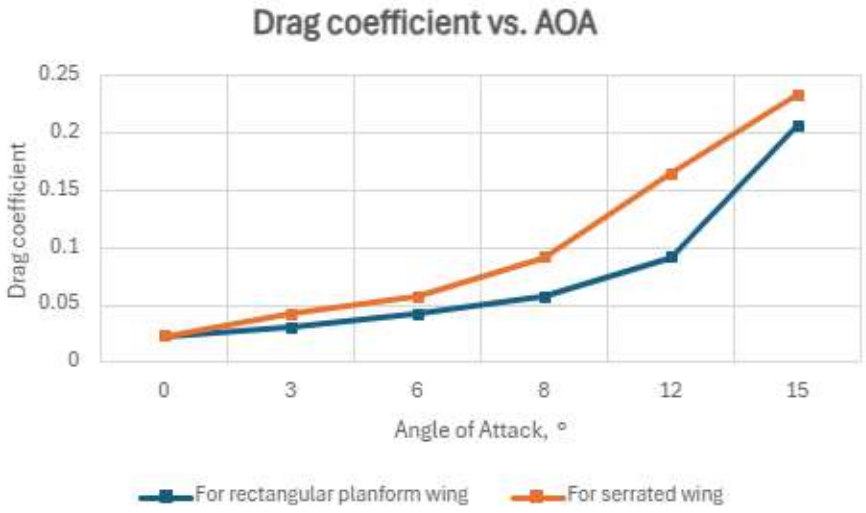

Figure 4.11: Drag coefficient vs Angle of Attack for both wings

It can be inferred from the Figure 4.9 that ratio of lift to drag is bigger for serrated wing than for rectangular planform wing at lower angles of attack. In contrast, for angle of attack bigger than 6°rectangular wing has bigger lift to drag ratio than serrated wing. Consequently, lift benefits from serrated wing at lower angles of attack and it benefits from rectangular wing at angles of attack bigger than 6°.

Evidently, serrated wing provides bigger lift coefficient than rectangular planform wing at all angles of attack (Figure 4.10). However, drag coefficient of serrated wing is also bigger than that of planform wing (Figure 4.11). Taking both of the graphs under consideration, difference in lift coefficients of rectangular wing and serrated wing is bigger than difference of drag coefficients of the wings (Figures 4.10- 4.11). That is why, it can be inferred from the abovementioned graphs that serrated wing is more productive in creating lift than rectangular planform wing.

4.7 CFD Analysis

Computational Fluid Dynamics analysis was performed in the ANSYS software (Figures 4.12- **??**). The lift coefficient closely aligns with experimental results up to AOA = 8°, indicating that the CFD simulation setup is well-calibrated in the attached-flow regime (Figure 4.14). However, the lift coefficient continues linear increase, reaching a value of 1.46 at AOA = 15°, while experimentally it was obtained to be around 0.71. Such a considerable difference could be attributed to the CFD k-omega turbulence model not fully capturing the transition-to-turbulence effects seen in real-life wind turbines. Nonetheless, the drag coefficient from CFD closely matches experimental data across the entire AOA range (Figure 4.15). This suggests that flow separation and wake behavior are being captured accurately enough in terms of total energy loss, even if the lift forces are slightly overpredicted at higher AOAs. The velocity magnitude contour at 5° AOA and 5 m/s wind speed shows strong agreement with experimental visuals (Figure 4.12- 4.13), as both exhibit wingtip vortices and vortex shedding, confirming that the CFD setup captures the major unsteady flow features even at moderate AOAs. Interestingly, this vortex shedding is revealed to be asymmetric in vorticity iso-surface plot.

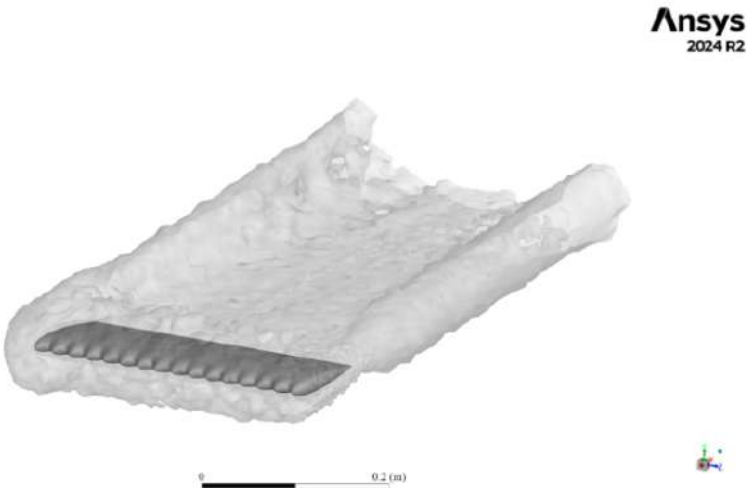

Figure 4.12: Vorticity iso-surfaces showing asymmetric wake vortex shedding (5 AOA, 5 m/s wind speed), transparent view

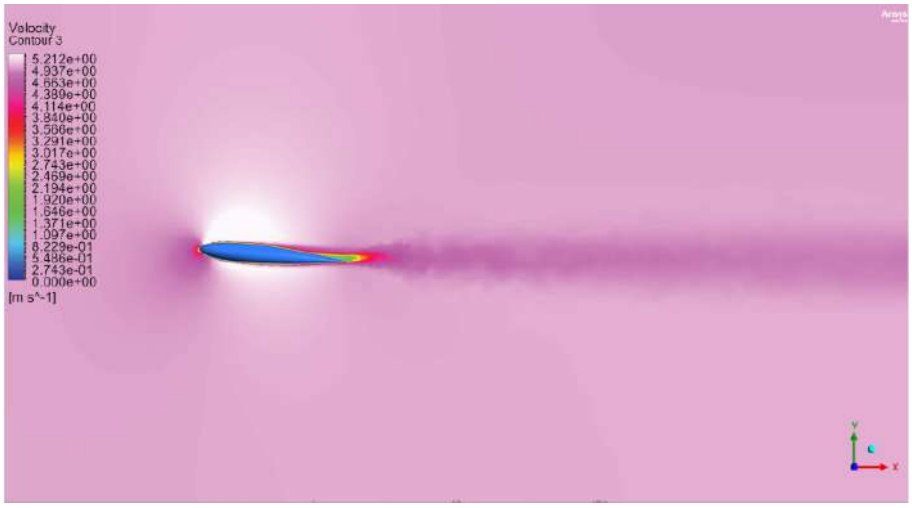

Figure 4.13: Velocity Contours of a flow around serrated wing, at windspeed 5 m/s and Angle of Attack 5°

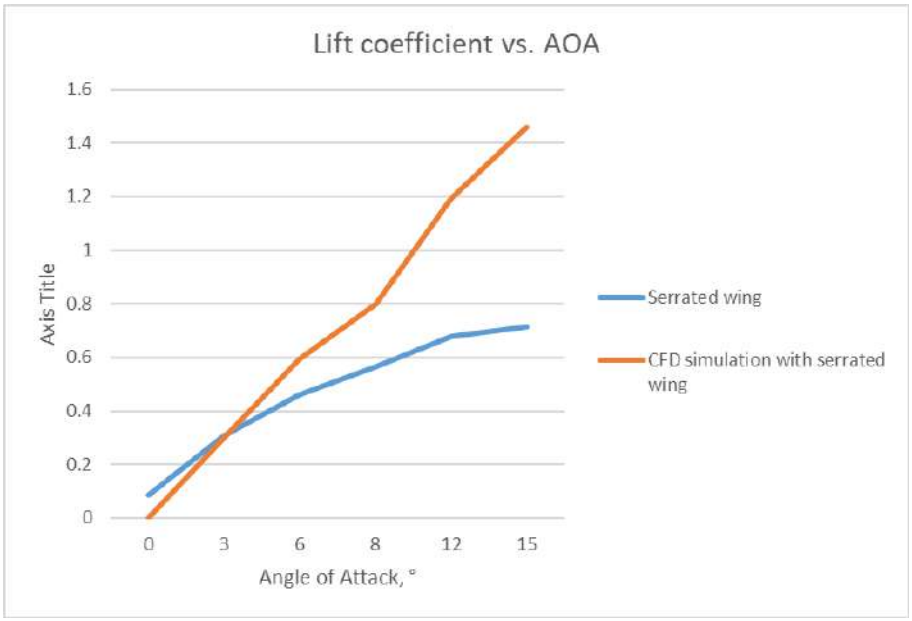

Figure 4.14: Lift coefficient vs Angle of Attack for experimental and CFD measurements

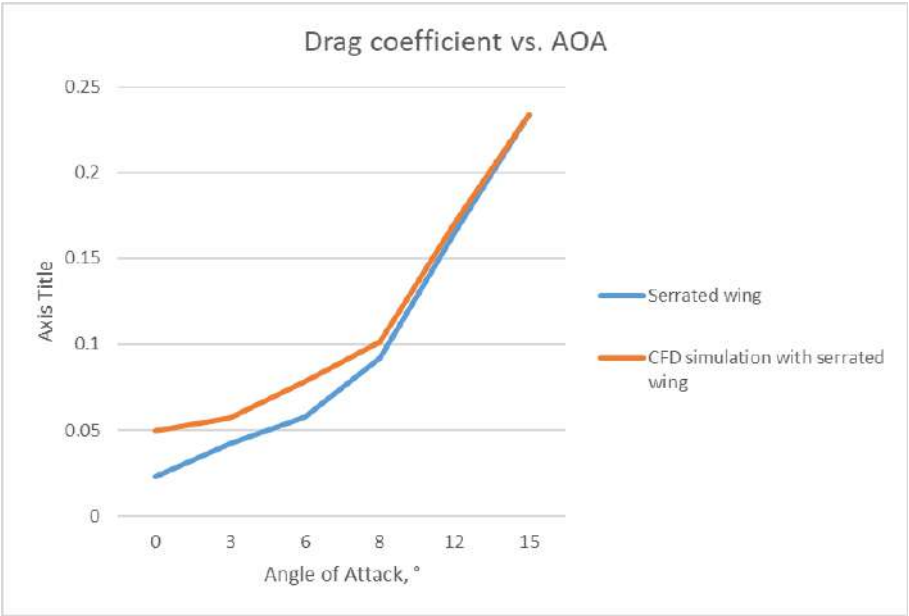

Figure 4.15: Drag coefficient vs Angle of Attack for experimental and CFD measurements

Chapter 5

Conclusion

5.1 Conclusion

5.1.1 PIV System Setup

Overall, all the main objectives of this project were achieved. The PIV system was set up in order to obtain the desired results. The system was calibrated and made functional, including the positioning of the particle generator and the positioning and focus of the camera. Positioning of the top and bottom mirrors in the same plane was also crucial to obtain flow visualization in the desired plane. Since the laser sheet is reflected from the bottom mirror, the location of bottom mirror defined the position of the laser sheet. Positioning of smoke generator was important as well: the smoke had to be in the same plane as laser sheet in order to get clear and informative images. Some items were purchased that benefited the setup. Mirror holder and lab grade mirrors are examples of such items. The adjustable table was designed and constructed. This is how one of the main aims of the project has been achieved: the PIV system was made functional. Safety precautions were taken into consideration and were strictly adhered to during experiments in the wind tunnel laboratory.

5.1.2 Flow Visualization

In addition, the PIV images of the particle flow were obtained for planform rectangular NACA 0012 airfoil and for the serrated wing of the same base profile. Insight 4G software was used in order to obtain visualization of the particle flow. Image pre-processing was performed: images were inverted and colored for better visibility. It was concluded that vortices that are generated in the flow around both planform rectangular wing and serrated wing are mushroom shaped. In both wings the flow is laminar at the speed 1.3 m/s, transitional at speeds in the range from 2 to 4 m/s, and turbulent in the range from 5 to 7 m/s. Vortices were much larger at the angle of attack equal to 5°than at zero angle of attack for both wings. In the flow around a serrated wing, vortices are tilted towards the wing. That was attributed to characteristics of serrated wing.

5.1.3 Aerodynamic Performance Analysis

Aerodynamic performance analysis was conducted during this research, namely, ratio of lift to drag, lift coefficient, and drag coefficient were plotted against angle of attack for both planform wing and serrated wing. It was concluded from the graphs of lift coefficient against angle of attack and drag coefficient against angle of attack that serrated wing is more productive at creating lift than planform rectangular wing. Graph of ratio of lift to drag against angle of attack was inconclusive.

5.1.4 CFD Analysis

The CFD simulation provides a comprehensive validation of the aerodynamic performance and behavior of the serrated NACA 0012 airfoil at a relatively low Reynolds number. While drag predictions are accurate, the overprediction of lift at higher AOAs highlights known CFD limitations in stall modeling. Additionally, vortex structures observed in contours and iso-surfaces closely match experiments.

5.2 Future Work

5.2.1 Serrated Wing Design

The serrated wing with the wavelength of 20 mm was printed and tested during the project experiments. The design used in this project is basically an airfoil with the leading-edge serrations. As part of future improvements to this study, some new designs with larger wavelengths or with trailing edge serrations can be printed and analyzed. Moreover, a wing with leading edge serrations of different other parameters (amplitude, wavelength) can be designed. Several wings with leading edge serrations can be designed and their aerodynamic performance can be compared with each other. That way, it would be possible to study the effect of amplitude and wavelength of serrations on aerodynamic performance of serrated wing. Possibly, optimal amplitude and wavelength can be found for NACA0012 profile.

5.2.2 Velocity Field Analysis

Although high-quality images were obtained from the PIV system, the velocity field analysis needs improvement, particularly in particle seeding quality. While the seeding density was improved to avoid particle overlap, ensuring sufficient coverage of the flow field, the particle size could be improved for better detection by software. Additional trials with adjustments of seeding material and dispersing methods can help determine the optimal particle dimensions for accurate measurements.

To further improve the accuracy of particle displacement in terms of software application, point processing could be considered for the new serrated wing designs, allowing analysis of one interrogation spot at a time. Further vector field evaluation and processing can be performed in the TecPlot software, included in Insight 4G. The processed velocity vector fields can then be used to generate visualizations of the flow around the wing tips. These visualizations would allow for a qualitative comparison of the flow characteristics associated with different wing designs, revealing insights into the aerodynamic effects of trailing-edge-serrated wings configurations.

5.2.3 Vortex Visualization and Validation

The next step would be to incorporate three-dimensional PIV (3D-PIV) to fully capture the vortex structure in the spanwise direction and the flow evolution in the near-field. This would provide more complete data on vortex interaction, secondary vortices, and the influence of surface roughness and geometry on vortex characteristics. 3D-PIV would enable capturing the three-dimensional dynamics of vortex roll-up and the influence of angle of attack on vortex morphology more effectively.

5.2.4 High-Resolution Computational Fluid Dynamics (CFD) Integration

To complement the experimental work, the integration of high-resolution CFD simulations with PIV data would allow a better understanding of the vortex's formation and its interaction with the flow. Advanced turbulence models, such as Large Eddy Simulation (LES) or Detached Eddy Simulation (DES), could be used in conjunction with laser visualization to validate vortex core measurements, pressure distribution, and wake evolution. The CFD results could provide insights into the effects of varying Reynolds numbers, different wing tip shapes, and angles of attack.

Bibliography

[1] C. M. Jurasz and V. P. Jurasz, "Feeding modes of the humpback whale, *Megaptera novaeangliae*, in southeast alaska," *Scientific Reports of the Whales Research Institute*, vol. 31, pp. 69–83, 1979.

[2] F. E. Fish and J. M. Battle, "Hydrodynamic design of the humpback whale flipper," *Journal of Morphology*, vol. 225, no. 1, pp. 51–60, 1995.

[3] F. E. Fish and G. V. Lauder, "Passive and active flow control by swimming fishes and mammals," *Annual Review of Fluid Mechanics*, vol. 38, pp. 193–224, 2006.

[4] D. Miklosovic, M. Murray, L. Howle, and F. Fish, "Leading-edge tubercles delay stall on humpback whale (megaptera novaeangliae) flippers," *Physics of fluids*, vol. 16, no. 5, pp. L39–L42, 2004.

[5] Scharnowski and Kähler, "Particle image velocimetry - Classical operating rules from todays perspective," *Optics and Lasers in Engineering*, vol. 135, 2020.

[6] J. D. Anderson, *Fundamentals of Aerodynamics*. McGraw-Hill, 4th ed., 2001. Standard reference for aerodynamic theory, including induced drag.

[7] J. Hunt, "Vorticity and Vortex Dynamics in Complex Turbulent Flows," *Transactions of the Canadian Society for Mechanical Engineering*, vol. 11, no. 1, 1987.

[8] U. Hussain, S. U. Malook, B. Shabir, O. Ali, and S. M. Ahmad, "Effect of trailing edge serration on the lift and drag characteristics of naca0012 airfoil wing," in *35th AIAA applied aerodynamics conference*, p. 4470, 2017.

[9] J. Westerweel, G. E. Elsinga, and R. J. Adrian, "Particle Image Velocimetry for Complex and Turbulent Flows," *The Annual Review of Fluid Mechanics*, 2012.

[10] J. E. Guerrero, C. Pacioselli, J. O. Pralits, F. Negrello, P. Silvestri, A. Lucifredi, and A. Bottaro, "Preliminary design of a small-sized flapping UAV: I. Aerodynamic performance and static longitudinal stability," *Meccanica*, vol. 51, p. 1343–1367, 2016.

[11] N. H. Hassan, M. H. Zawawi, A. M. M. A. Bakri, Z. M. R. Rozainy, M. A. Kamaruddin, W. N. Y. W. M. Nasir, M. A. N. Mazlan, and A. R. Irfan, "A Review on Applications of Particle Image Velocimetry," *IOP Conf. Series: Materials Science and Engineering*, vol. 864, 2020.

[12] T. H. New, J. Long, B. Zang, and S. Shi, "Collision of vortex rings upon V-walls," *J. Fluid Mech*, vol. 899, 2020.

[13] A. Khalaf and J. Kennedy, "The dual impact of winglets and serrations on uav aerodynamic and acoustic performance," *Drones*, vol. 9, no. 4, p. 302, 2025.

[14] Y. Li, Y. Yang, Y. Liu, Y. Wang, B. Huang, and W. Li, "Aerodynamic and aeroacoustic analyses of a uav propeller with trailing edge serrations," in *Proceedings of ACOUSTICS 2018*, pp. 1–10, 2018.

[15] D. H. Freedman, "An Unexpected Twist Lights Up the Secrets of Turbulence," *Quantamagazine*, 2020.

[16] M. Coletta, F. D. Gregorio, A. Visingardi, and G. Iuso, "PIV data: Vortex Detection and Characterization," *13th International Symposium on Particle Image Velocimetry*, 2019.

[17] Z. Gao, J. Wang, J. Wang, Y. Mao, and Y. Wei, "Analysis of the effect of vortex on the flow field of a cylindrical cyclone separator," *Separation and Purification Technology*, vol. 211, p. 438–447, 2019.

[18] L. Graftieaux, M. Michard, and N. Grosjean, "Combining PIV, POD and vortex identification algorithms for the study of unsteady turbulent swirling flows," *Measurement Science and Technology*, vol. 12, 2001.

[19] H. Liu, S. Wang, and T. Liu, "Vortices and forces in biological flight: Insects, birds, and bats," *Annual Review of Fluid Mechanics*, vol. 56(1), pp. 147–170, 2024.

[20] F. T. Muijres, L. C. Johansson, Y. Winter, and A. Hedenström, "Leading edge vortices in lesser long-nosed bats occurring at slow but not fast flight speeds," *Bioinspiration and biomimetics*, vol. 9(2), 2014.

[21] L. Chen, B. Cheng, and J. Wu, "Vorticity dynamics and stability of the leading-edge vortex on revolving wings," *Physics of Fluids*, vol. 35(9), 2023.

[22] K. Warfvinge, L. C. Johansson, and A. Hedenström, "Hovering flight in hummingbird hawkmoths: kinematics, wake dynamics and aerodynamic power," *Journal of Experimental Biology*, vol. 224(10), 2021.

[23] L. G. Liu, G. Du, and M. Sun, "Aerodynamic-force production mechanisms in hovering mosquitoes," *Journal of Fluid Mechanics*, vol. 898, A19, 2020.

[24] M. Shorbagy, B. El-hadidi, G. El-Bayoumi, O. Said, and M. Fouda, "Experimental study on bio-inspired wings with tubercles," in *AIAA Scitech 2019 Forum*, p. 0848, 2019.

[25] N. Rostamzadeh, R. M. Kelso, and B. Dally, "A numerical investigation into the effects of reynolds number on the flow mechanism induced by a tubercled leading edge," *Theoretical and Computational Fluid Dynamics*, vol. 31, pp. 1–32, 2017.

[26] A. Asghar, R. E. Perez, and M. Ferchichi, "Effect of leading edge tubercles on transonic performance of airfoils," in *35th AIAA Applied Aerodynamics Conference*, p. 3402, 2017.

[27] C. Cai, Z. Zuo, T. Maeda, Y. Kamada, Q. Li, K. Shimamoto, and S. Liu, "Periodic and aperiodic flow patterns around an airfoil with leading-edge protuberances," *Physics of fluids*, vol. 29, no. 11, 2017.

[28] D. Custodio, "The effect of humpback whale-like leading edge protuberances on hydrofoil performance," *Worcester Polytechnic Institute*, vol. 75, 2007.

[29] M. D. Bolzon, R. M. Kelso, and M. Arjomandi, "Formation of vortices on a tubercled wing, and their effects on drag," *Aerospace Science and Technology*, vol. 56, pp. 46–55, 2016.

[30] K. Liu, B. Song, D. Xue, W. Yang, A. Chen, and Z. Wang, "Numerical study of the aerodynamic effects of bio-inspired leading-edge serrations on a heaving wing at a low reynolds number," *Aerospace Science and Technology*, vol. 124, p. 107529, 2022.

[31] M. Sakai, Y. Sunada, and K. Rinoie, "Three-dimensional separated flow on a flat plate with leading-edge serrations," in *53rd AIAA Aerospace Sciences Meeting*, p. 0047, 2015.

[32] A. Winzen, B. Roidl, S. Klän, M. Klaas, and W. Schröder, "Particle-image velocimetry and force measurements of leading-edge serrations on owl-based wing models," *Journal of Bionic Engineering*, vol. 11, no. 3, pp. 423–438, 2014.

[33] T. Ikeda, T. Ueda, T. Nakata, R. Noda, H. Tanaka, T. Fujii, and H. Liu, "Morphology effects of leading-edge serrations on aerodynamic force production: An integrated study using piv and force measurements," *Journal of Bionic Engineering*, vol. 15, pp. 661–672, 2018.

[34] B. Cranston, C. Laux, and A. Altman, "Leading edge serrations on flat plates at low reynolds number," in *50th AIAA Aerospace Sciences Meeting including the New Horizons Forum and Aerospace Exposition*, p. 53, 2012.

[35] TecQuipment Ltd, *AF1600 Subsonic Wind Tunnel User Guide*, 2017.

[36] Litron Lasers Ltd, *LAS040-LPY PIV User Manual*, 3rd ed., 2019.

[37] TSI Incorporated, *Oil Droplet Generators Models 9307 and 9307-6*, 2015.

[38] TecQuipment Ltd, *AFA10 Smoke Generator User Guide*, 2017.

[39] TecQuipment Ltd, *AF1600t with AFA4 Three Component Balance with Balance Angle Feedback User Guide*, 2018.

[40] TSi Incorporated, *INSIGHT 4G. Global Image Acquisition, Analysis and Display Software Tutorial Guide*, 2015.

[41] A. A. Molaa and M. A. Abdulwahid, "Numerical and experimental study of the impact on aerodynamic characteristics of the naca0012 airfoil," *Open Engineering*, vol. 14, no. 1, p. 20220506, 2024.

[42] A. Uzun, M. Y. Hussaini, and C. L. Streett, "Large-eddy simulation of a wing tip vortex on overset grids," *AIAA journal*, vol. 44, no. 6, pp. 1229–1242, 2006.

Appendices

Appendix A

The First Appendix

A.1 Non-Inverted Images

Figure A.1: Non-inverted PIV image of the particle flow at 1.3 m/s

Figure A.2: Non-inverted PIV image of the particle flow at 2 m/s

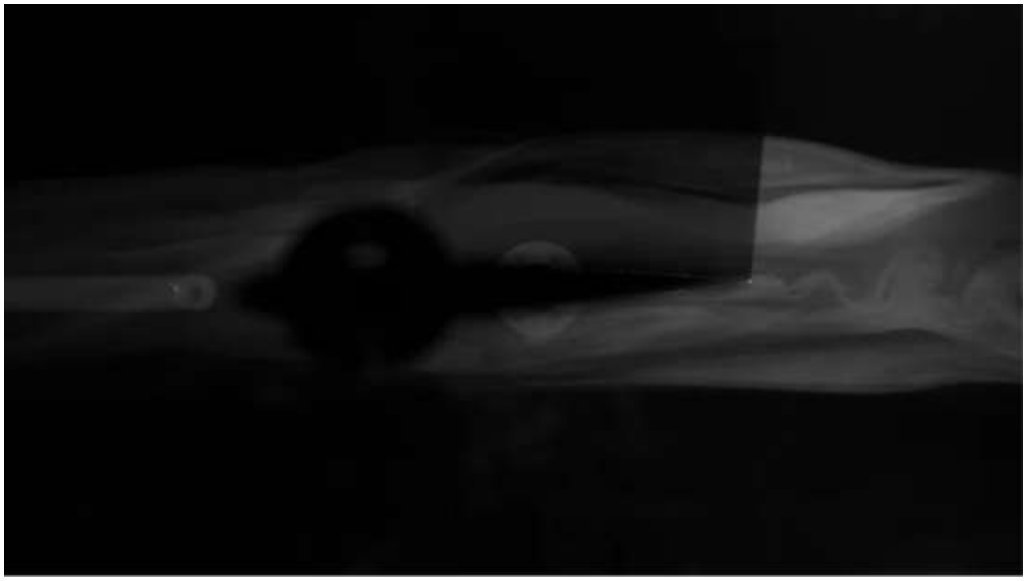

Figure A.3: Non-inverted PIV image of the particle flow at 3 m/s

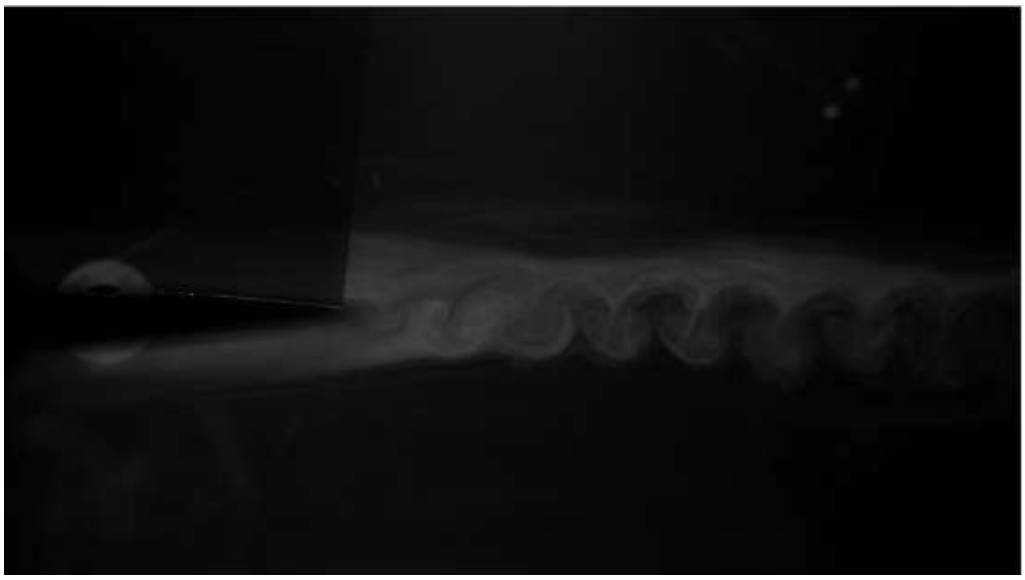

Figure A.4: Non-inverted PIV image of the particle flow at 5 m/s

Figure A.5: Non-inverted PIV image of the particle flow at 6 m/s

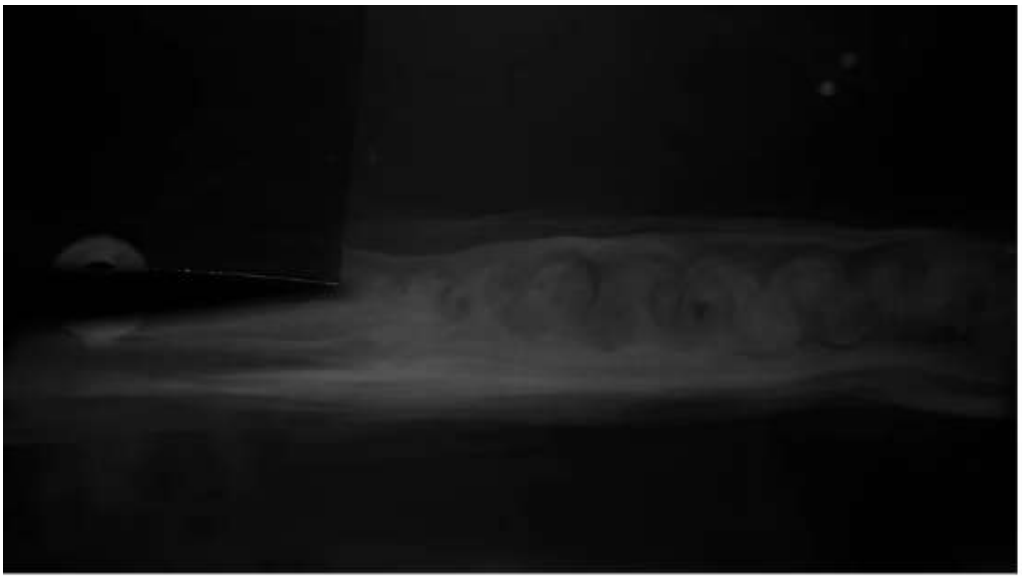

Figure A.6: Non-inverted PIV image of the particle flow at 7 m/s

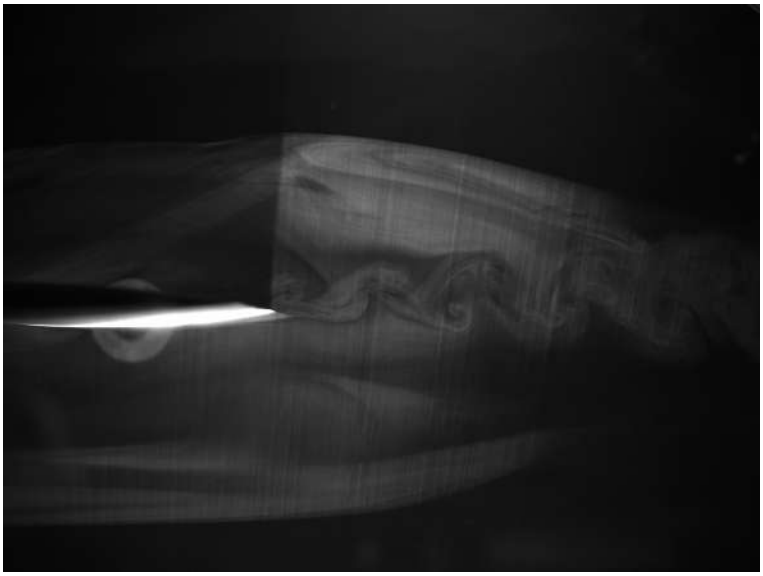

Figure A.7: Non-inverted PIV image of the particle flow around the serrated wing at 2 m/s

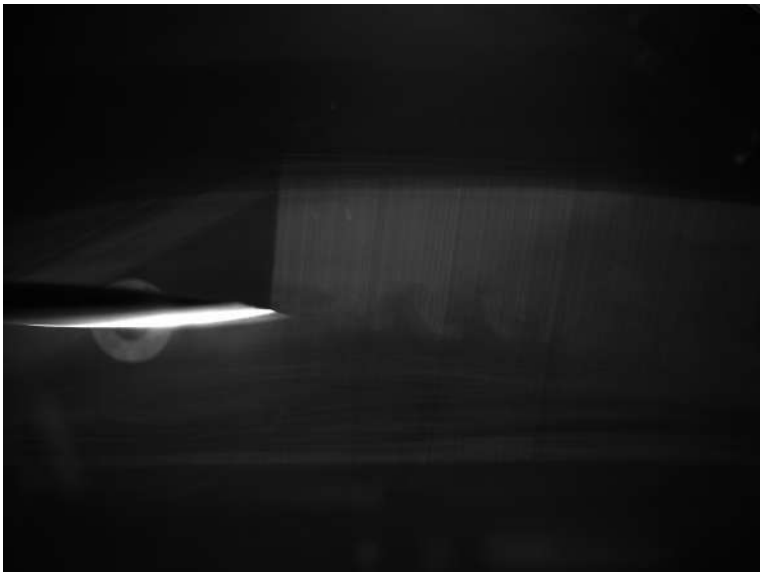

Figure A.8: Non-inverted PIV image of the particle flow around the serrated wing at 3 m/s

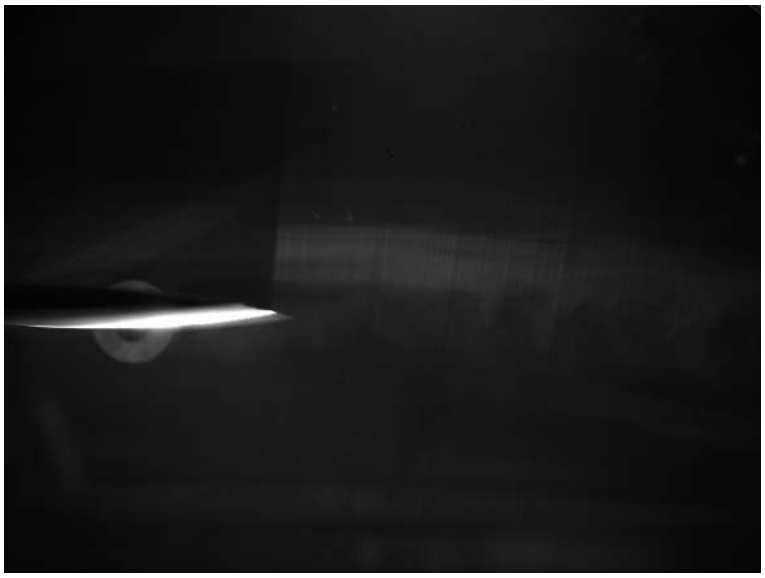

Figure A.9: Non-inverted PIV image of the particle flow around the serrated wing at 4 m/s

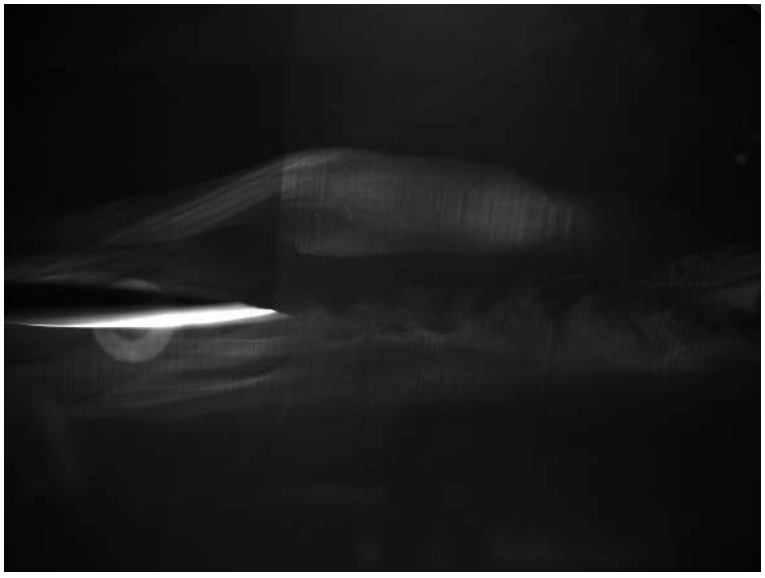

Figure A.10: Non-inverted PIV image of the particle flow around the serrated wing at 5 m/s

Figure A.11: Non-inverted PIV image of the particle flow around the serrated wing at 6 m/s

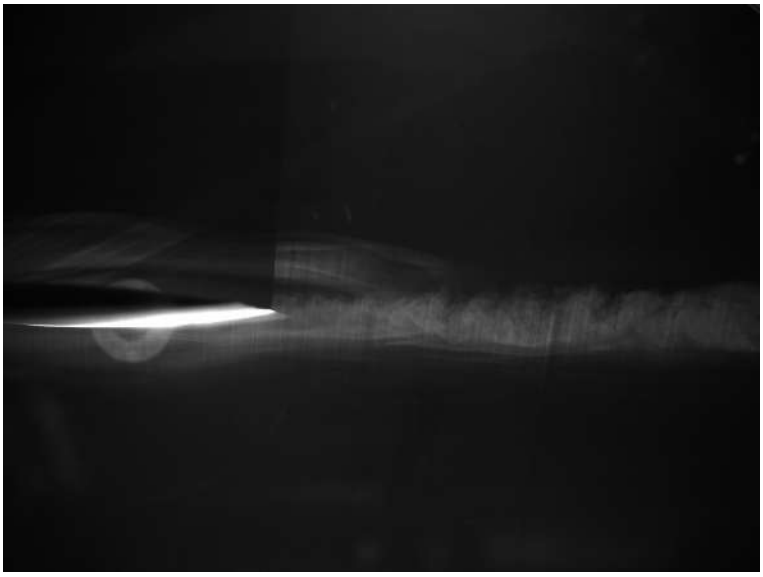

Figure A.12: Non-inverted PIV image of the particle flow around the serrated wing at 7 m/s